PHYSICAL REVIEW E 98, 032411 (2018)

Role of fluid-structure interaction in generating the characteristic tip path of a flapping flexible wing

D. Ishihara

Department of Mechanical Systems Engineering, Kyushu Institute of Technology, 680-4 Kawazu, Iizuka, Fukuoka 820-8502, Japan

ABSTRACT

This study shows that the characteristic modes, such as the figure-eight mode, can be created in the path of the wingtip, which is caused by the fluid-structure interaction, using a flapping model wing with two lumped flexibilities describing the elevation motion as well as the pitching motion. A direct numerical simulation based on the three-dimensional finite element method for fluid-structure interaction (FSI) analyzes the behaviors of the model wing, the surrounding air, and their interaction, where the dynamic similarity law for the FSI is used to incorporate actual insect data, and the parallel computation algorithm is used to perform the systematic parametric study. Characteristic modes, such as the figure-eight mode, are observed in the path of the wingtip from the elevation motion of the simulated wing. This motion is considered as the forced vibration caused by the interaction with the surrounding fluid excited by the flapping of the wing. Therefore, this motion can be modulated by the flexibility to change the natural frequency, which can be controlled by the muscles at the base of the wing in the actual insect. The present simulation shows that the selection between these modes in the path of the wingtip depends on the ratio between the natural frequency of the elevation motion and the flapping frequency. In the case of the figure-eight, the upward elevation motion of the wing acts on the leading edge vortex (LEV) so as to keep its momentum upon stroke reversal. Therefore, this LEV can remain in the wake of the wing after stroke reversal and enhance the next LEV. Because of this effect, the lift increases significantly as the mode of the wingtip path shifts to the figure-eight mode. This understanding will contribute to a developed field of bio-inspired micro air vehicles, i.e. it will reduce the complexity of electromechanical devices that prescribe entire motions of their wings.

1. INTRODUCTION

Approximately 300 million year ago, insects were the first organisms on Earth to take to the sky, which was a momentous evolutionary step [1]. The advantages of flight over other forms of locomotion resulted in the dispersal of insects all over the world. Their flight

abilities have become increasingly refined throughout their long period of development. Their flapping wings exhibit characteristic motions in flight [2]. Therefore, it is important to reveal the role of the wing motion in generating enough lift [3] and the mechanism of its creation [4].

Many researchers have considered the path of the wingtip relative to the body or the wingtip path. Early research reported that this path forms a figure-eight (mode of two-loop with one-crossing), and subsequent studies reported that the path can also take other characteristic modes, such as a three-loop with two-crossing or a four-loop with three-crossing [1, 2, 5-10]. The mode shift can be controlled according to the airstream over the antennae [5], while the wingtip path may be indirectly altered by changes in articulation at the wing base, which control flapping parameters such as the stroke angle [2]. Most recently, it was shown through a dynamically scaled experiment that the figure-eight mode resulted in a lift increase [11]. Furthermore, electromechanical devices for active generation of the figure-eight mode have been designed and fabricated for micro air vehicles (MAVs) [12-14].

Ref. [15] mentioned the possibility of the wing-hinge compliance to allow the wing's elevation motion for bio-inspired MAVs [16]. In the present study, the mechanism that creates the characteristic wingtip path is investigated from the viewpoint of the vibration theory.

The insect flapping flight system consists of hierarchical subsystems with different length and time scales from anatomical, physiological, ecological, energetic, and mechanical perspectives. Therefore, because of the complexity of this composite system, its decomposition into subsystems is useful in order to understand the specific mechanism. The articulation at the wing base consists of steering muscles, tendons, and both flexible and rigid components. This articulation works as a transmission that redirects power from the flight muscles to the wing and allows control over its motion [17-20]. However, the mechanism of this transmission remains unclear due to the complexities of the interactions with other subsystems as well as its own dynamics.

In the present study, the articulation at the wing base is expressed as a reduced-order model using the lumped flexibilities, where the articulation providing the adequate flexibilities is described as the macroscopic constitutive relationship between the force and the deformation. The lumped flexibility model [21-36] has been gaining popularity to consider the flexibility of the insect wing, which is one of most important features of the insect wing, while to avoid the aforementioned complexities. Typically, this model has been used to describe the pitching motion of the wing. The high torsional flexibility of the insect wing suggests the passivity of the pitch motion [4, 38]. The evidence from a mechanical point of view was first presented demonstrating the inertial cause of the wing rotation using the two-dimensional rigid wing [37, 39]. Then, an elastic spring was introduced as the torsional flexibility, and this model demonstrated that the basic pattern of the pitch motion can be caused by the fluid-structure interaction [15, 21, 22]. This type of model or the lumped torsional flexibility model is also useful for discussing the effect of the torsional

flexibility on the lift generation [31-33, 36]. This type of model introduced a three-dimensional wing in order to consider the three-dimensional effect [25, 26, 29, 35]. The role of the torsional flexibility in flapping locomotion was investigated using this type of model [23, 30]. The maneuver mechanism based on the mechanical properties of the wing's hinge was explained using this type of model [24, 40]. In contrast, in the present study, this model is extended to describe the elevation motion of the wing from the stroke plane as well as the pitching motion of the wing.

Most recently, numerical fluid-structure interaction analysis has been used in studies on insect flapping flight [22, 25, 28, 41, 42]. Some studies have reported three-dimensional simulations of flexible wings using numerical fluid-structure interaction analysis in order to take into account the three-dimensional effects [34, 42-45]. In the present study, three-dimensional finite element analysis for the interaction of an incompressible viscous fluid and an elastic body [46, 47] is used to accurately simulate the behavior of the model wing in air [25]. This direct numerical simulation is guided by the dynamic similarity law for the fluid-structure interaction (FSI) [26] such that the model wing is dynamically similar to the actual insect wing. The parallel computation algorithm is introduced to the present numerical FSI analysis method in order to reduce the computational time associated with the systematic investigation.

The simulation results of the present study show that the characteristic wingtip path modes, including the figure-eight mode, can be created by the fluid-structure interaction. The motion is considered as the forced vibration caused by the interaction with the surrounding air excited by the wing's flapping. Therefore, the compliance of the wing's elevation modulates the elevation motion by changing the natural frequency, and the selection between the modes in the path of the wingtip depends on the ratio between the natural frequency of the elevation motion and the flapping frequency.

The upward elevation motion of the wing in the figure-eight mode acts on the leading edge vortex (LEV) so as to keep its momentum upon stroke reversal. Therefore, this LEV can remain in the wake of the wing after stroke reversal and enhance the new LEV at the beginning of the next half-stroke. Because of this effect, the lift increases significantly as the mode shifts from a higher mode to the figure-eight mode. Let us recall the passivity of the mode creation and the mode selection using the compliance of the wing's elevation. It follows from these results that the insect can take the specific modes of the wingtip path automatically by changing the compliance of the wing's elevation in order to control the lift.

2. WING MODEL AND NUMERICAL METHOD

2.1 Lumped flexibility model

The lumped flexibility model, which is based on the macroscopic constitutive relationship [21], has been used in studies related to the passivity of the wing's pitching motion [15, 21-23, 34]. In the present study, as shown in Figure 1, this model is extended so as to allow the wing's elevation motion from the stroke plane. In this section, the conventional model is

described and is then extended to have lumped flexibility for the wing's elevation.

2.1.1 Lumped torsional flexibility model

The lumped torsional flexibility is expressed schematically using a spring, as shown in Figures 1 and 2 (a). The objective of this is to simplify the complicated elastic behavior of insect wings to the fundamental pitching mode to investigate the passive pitching kinematics caused by the inertial, aerodynamic, and elastic torques [21][22]. The basis for this in nature is as follows:

A high torsional flexibility at the base of an insect wing [4, 38] leads to a high angle of attack that separates the air flow around the wing and creates a leading-edge vortex that provides sufficient lift for the insect to maintain flight. However, twist and camber are relatively small [48, 49, 67], and flow separation is not very sensitive to such deformations [50]. Therefore, as a first approximation, an insect wing and its flexibilities can be modeled using a rigid flat-plate wing and springs, respectively. This type of model [15, 21-26, 30-32, 34, 51] as well as the rigid flat-plate wing model [3, 39, 52-64] has recently gained popularity.

The wing base is placed at the origin O of a Cartesian coordinate system. The horizontal x-axis is positive in the forward direction of the longitudinal axis of the insect body. An ideal hovering state is assumed in the present study. The stroke plane is set in the horizontal xz plane, because it is approximately horizontal in many hovering insects [65]. The flapping axis is defined as the vertical y-axis. The angular displacement of the flapping motion φ ($-\Phi/2 \leq \varphi \leq \Phi/2$, where Φ is the stroke plane angle) is defined as the angle between the leading edge of the wing and the z-axis and is positive for counterclockwise rotation about the y-axis. The axis of the torsion is placed along the leading edge, which runs from the base to the tip of the wing. The pitch angular displacement θ is defined as the angle between the wing chord and the vertical direction and is positive for counterclockwise rotation about the torsional axis. Torsional flexibility can be characterized by the compliance of the torsion C_θ [38], which is defined as the ratio of θ to the applied moment around the axis of the torsion. The mean aerodynamic force acting on the wing is dependent on the nondimensional radius r_2 of the second moment of the wing area [66, 67]. In many insects, r_2 is very close to that of a rectangular wing at $1/\sqrt{3}$ [48, 67]. Therefore, for the sake of simplicity, a rectangular wing model is used. Its planar shape can be defined in terms of aspect ratio r_A ($= 2L_w/c_m$, where L_w is the span length of one wing, and c_m is the mean chord length).

The initial state of the wing chord is set to be at rest and oriented vertically (normal to the stroke plane). The time variation of φ is close to sinusoidal but has a larger acceleration or deceleration during stroke reversals and a constant velocity during the middle of each half-stroke [2]. Therefore, $d\varphi/dt$ can be expressed as a trapezoidal function, as shown in Figure 3, where the acceleration or deceleration time t_a is used to define the period of increasing or decreasing of the flapping velocity in each cycle. In the present study, t_a^u for the upstroke and t_a^d for the downstroke, which can express the difference in flapping motion between the upstroke and the downstroke, are newly introduced. The flapping period T_φ is

the inverse of the flapping frequency f_φ. The initial value of φ is set to $-\Phi/2$. $\mathbf{F}_S$ is the total fluid surface force acting on one wing nondimensionalized by the dynamic pressure $\rho^f A_w V_m^2/2$, where ρ^f is the fluid density, A_w is the area of one wing, and V_m is the mean flapping velocity, which is defined as $2r_2\Phi L_w f_\varphi$. The nondimensional lift F_L is defined as the y-component of $\mathbf{F}_S$, and the nondimensional drag F_D is defined as the inner product of $\mathbf{F}_S^*$ and $\mathbf{n}^*$, where $\mathbf{F}_S^*$ is the projection of $\mathbf{F}_S$ onto the stroke plane, $\mathbf{n}$ is the unit vector normal to the upper surface of the wing, and $\mathbf{n}^*$ is the projection of $\mathbf{n}$ onto the stroke plane.

2.1.2 Extension of lumped torsional flexibility model

The flexibility of the wing with respect to elevation from the stroke plane is modeled using the lumped flexibility at the base of the wing, which is expressed schematically as a spring, as shown in Figure 1. The elevation angular displacement χ is defined as the angle between the axis of torsion and its projection onto the stroke plane and is positive when the wing is over the stroke plane. The axis of the elevation is placed in the stroke plane and is normal to the axis of torsion. The lumped flexibility for the elevation is characterized by the compliance of the elevation C_χ, which is defined as the ratio of χ to the applied moment around the axis of the elevation.

2.1.3 Implementation of lumped torsional flexibility model

As shown in Figure 2, the plate spring is the implementation of the lumped torsional flexibility expressed schematically by the torsional spring, and is used to allow for passive rotation of the wing plate.

The motivation of this is the accuracy of the numerical analysis for the flapping wing in fluid. In contrast to the case of the torsional spring, the finite element modeling error is very small. Therefore, the present finite element method has been sufficiently validated using the corresponding dynamically scaled experiment [25][28].

The plate spring is set in Section 2.6 such that it works as the lumped torsional flexibility, i.e. it simplifies the complicated elastic behavior of insect wings to the fundamental pitching mode. The result to show this consistency is described in APPENDIX.

2.2 Governing equations

The interaction between the flexible wing and the surrounding fluid can be described by the three-dimensional partial differential equations of motion for an elastic body, the three-dimensional incompressible Navier–Stokes (NS) equations for a fluid, and the compatibility and equilibrium conditions for a fluid-structure interface [68].

The equilibrium equation for an elastic body can be expressed as

$$\rho^s \frac{\mathrm{d}v^s{}_i}{\mathrm{d}t} = \frac{\partial \sigma^s{}_{ji}}{\partial x_j}, \qquad (1)$$

where d/dt in the left-hand side is the Lagrangian time derivative, the superscript s indicates a quantity corresponding to the structure, ρ is the mass density, v_i is the ith component of the velocity vector, and σ_{ij} is the ijth component of the Cauchy stress tensor. The present wing consists of both stiff and flexible components, which can be expressed as a single elastic body. Therefore, the motion can be described by Eq. (1) with the adequate initial and boundary conditions. The active flapping motion is imposed as the time-dependent elementary boundary condition.

The incompressible NS equations using the arbitrary Lagrangian-Eulerian (ALE) method [69] can be expressed as

$$\rho^{\mathrm{f}} \frac{\partial v^{\mathrm{f}}{}_i}{\partial t} + \rho^{\mathrm{f}} (v^{\mathrm{f}}{}_j - v^{\mathrm{m}}{}_j) \frac{\partial v^{\mathrm{f}}{}_i}{\partial x_j} = \frac{\partial \sigma^{\mathrm{f}}{}_{ji}}{\partial x_j} \quad \text{and} \quad \frac{\partial v^{\mathrm{f}}{}_i}{\partial x_i} = 0, \qquad \text{(2a, b)}$$

where $\partial / \partial t$ in the left-hand side is the ALE time derivative, and the superscripts f and m indicate quantities corresponding to the fluid and the ALE coordinate systems, respectively.

The geometrical compatibility and equilibrium conditions can be expressed, respectively, as

$$v^{\mathrm{f}}{}_i = v^{\mathrm{s}}{}_i \quad \text{and} \quad \sigma_{ij}^{\mathrm{f}} n_j^{\mathrm{f}} + \sigma_{ij}^{\mathrm{s}} n_j^{\mathrm{s}} = 0 \qquad \text{(3a, b)}$$

where n_i is the ith components of the outward unit normal vector on the FSI corresponding to the fluid or the structure.

The damping from the air viscosity and the structure itself seems to be under-damping with damping ratio in the order less than 5% [70]. Therefore, it is assumed that the structural damping is ignorable in this study.

2.3 Dynamic similarity law for FSI

In the studies of insect flapping flight using the dynamically scaled model, the dynamic similarity law is used to correctly incorporate morphological and kinematical data from the actual insect into the model wing. Initially, the dynamic similarity law for the fluid dynamics was used for the experimental model [3, 52]. Most recently, the dynamic similarity law for the FSI was introduced in the numerical model [22], and then it was used for the experimental model [25, 26]. This dynamic similarity law is briefly summarized in the following, since it is used to guide the present direct numerical simulation:

The nondimensional parameter α, the Reynolds number Re, the Cauchy number Ca, and the mass ratio M are obtained by the dimensional analysis for the governing equation system of Eqs. (1) through (3) with respect to the characteristic length or the mean chord length c_{m}, the characteristic velocity or the mean flapping velocity V_{m}, and the characteristic time or the flapping frequency $T_\varphi = 1/f_\varphi$ as follows [25, 26, 28]:

$$\alpha = f_\varphi \, c_\mathrm{m}/V_\mathrm{m}, \tag{4a}$$

$$\mathrm{Re} = \rho^\mathrm{f} \, c_\mathrm{m} \, V_\mathrm{m}/\mu^\mathrm{f}, \tag{4b}$$

$$\mathrm{Ca} = \rho^\mathrm{f} \, V_\mathrm{m}^2 \, c_\mathrm{m}^3 \, \mathrm{C}_\theta, \tag{4c}$$

$$M = m_\mathrm{w}/(\rho^\mathrm{f} \, c_\mathrm{m}^3), \tag{4d}$$

where m_w is the mass of the wing. The expression (4d) in Refs. [71-73] was used, since the data for m_w is available from many literatures. The hovering state is assumed in this study. Therefore, the flow velocity can be characterized by the mean flapping speed V_m. The definition of V_m reduces the expression of α to $1/(r_2 r_\mathrm{A} \Phi)$. This parameter specifies the translational motion of the wing [59]. The similar parameter is also presented in Ref. [79]. These four nondimensional parameters can make two different FSI systems dynamically similar to each other.

2.4 Direct numerical simulation

The interaction between the flexible wing and the surrounding fluid can be described by the governing equations (1) through (3). In the present study, the projection method for the FSI [46, 47] is used to solve Eqs. (1) through (3) efficiently, which is briefly described as follows.

Applying finite element discretization to Eqs. (1) and (2), the nonlinear equilibrium equations can be obtained in matrix-vector form. Applying the interface conditions (3) to these equations, the monolithic equation system for the FSI can be obtained as

$$_\mathrm{L}\mathbf{M}\mathbf{a} + \mathbf{C}\mathbf{v} + \mathbf{N} + \mathbf{q}(\mathbf{u}) - \mathbf{G}\mathbf{p} = \mathbf{g}, \quad _\tau\mathbf{G}\mathbf{v} = \mathbf{0}, \tag{5a, b}$$

where **M**, **C**, and **G** are the mass, diffusive, and divergence operator matrices, **N**, **q**, **g**, **a**, **v**, **u**, and **p** are the convective term, elastic internal force, external force, acceleration, velocity, displacement, and pressure vectors, respectively, and subscripts L and τ indicate the lumping of the matrix and the transpose of the matrix, respectively.

Equations (5a) and (5b) are solved using the monolithic method [74], where the interface conditions are implicitly satisfied in order to avoid spurious numerical power on the interface, which yields numerical instability. However, this formulation leads to an ill-conditioned system of equations. Therefore, a projection method using algebraic splitting [46, 47] is used in order to avoid this difficulty. This method splits the monolithic equation system (5) into the following three equations:

$$\mathbf{M}^* \Delta\hat{\mathbf{a}} = \Delta\mathbf{g}, \tag{6}$$

$$\gamma \Delta t_\tau \mathbf{G}_{\mathrm{L}} \mathbf{M}^{-1} \mathbf{G} \Delta \mathbf{p} = -_\tau \mathbf{G} \hat{\mathbf{v}}, \tag{7}$$

$$\mathbf{M}^* \Delta \mathbf{a} - \mathbf{G} \Delta \mathbf{p} = \Delta \mathbf{g}. \tag{8}$$

where the pressure and elastic interior force terms are evaluated implicitly, $\hat{\mathbf{a}}$ is the intermediate acceleration, $\hat{\mathbf{v}}$ is the intermediate velocity, which is given by $\hat{\mathbf{a}}$, $\mathbf{M}^*$ is the generalized mass matrix, which is composed of the lumped mass matrix and the tangential stiffness matrix, Δ denotes the increment, t denotes the current time, $\Delta\mathbf{g}$ is the residual vector of Eq. (5a), and the relations among the state variables are based on Newmark's method. Equation (7) is the pressure Poisson equation. Solving this equation, the incompressibility constraint (5b) is satisfied implicitly.

In the nonlinear iteration of each time step, Eqs. (6) through (8) are solved to derive the intermediate velocity field, the current pressure field such that the current velocity field satisfies the incompressibility constraint, and the current velocity field, respectively.

2.5 Parallel computation based on mesh decomposition

In the present study, the parallel computation algorithm is introduced in order to reduce the computational time. The following matrix-vector product is the most expensive computation in an iterative solver:

$$_\tau \mathbf{G}_{\mathrm{L}} \mathbf{M}^{-1} \mathbf{G} \Delta \mathbf{p}^{(k)}, \tag{9}$$

where $\Delta\mathbf{p}^{(\mathrm{k})}$ is the solution vector at the kth iteration in the iterative solver. Assuming that the number of DOFs of the structure is far smaller than that of the fluid, we use the following parallel solution procedure based on the mesh decomposition. The mesh is decomposed as shown in Figure 4. The symbols Ω^{s} and Ω^{f} denote the structural and fluid meshes, respectively, and Ω^{f}_i (i = 1, 2, …, N_{d}) denotes ith submesh of Ω^{f}. Note that Ω^{f}_1 surrounds Ω^{s} so that the matrix-vector product concerning the fluid-structure interface can be computed at a single computational node. The computations related to Ω^{f}_i are executed at computational node P_i, while the computations related to Ω^{s} are executed at P_1. Under the above setup, the parallel computation of (9) is executed using the following steps.

(Step 1) The matrix-vector product (9) is computed at P_i using the element-by-element method as

$$\mathbf{A}\mathbf{p} = \sum_e \mathbf{A}^{(e)} \mathbf{p}^{(e)} = \sum_e \mathbf{q}^{(e)} = \mathbf{q}, \tag{10}$$

where **A** denotes the global matrix, **p** denotes the global vector, **q** denotes their matrix-vector product, $\mathbf{A}^{(e)}$ and $\mathbf{p}^{(e)}$ are their elemental counterparts, respectively, and e denotes the element number.

(Step 2) The nodal data of the matrix-vector product (9) on the interface between Ω^{f}_i and Ω^{f}_j ($j \neq i$) computed at P_j are transferred to P_i in order to complete the corresponding nodal data computed in Step 1.

The algorithm presented in this section is implemented using the Message Passing Interface (MPI) library.

2.6 Problem setup

Figures 5 and 6 show the finite element meshes of the model wing and the surrounding fluid domain, respectively. In Figure 5, the white domain is the plate spring corresponding to the concentrated torsional flexibility, the black domain is the plate spring corresponding to the concentrated elevation flexibility, the grey domain is the stiff wing plate, and the red domain is the stiff leading edge. As described in Section 2.3, two different FSI systems are dynamically similar to each other if the conditions of the nondimensional parameters α, Re, Ca, and M, as well as geometrical similarity, are satisfied. Therefore, these values are set as α = 0.07, Re = 260, Ca = 0.19, and M = 16, which are in the range of the values for actual insects [25], and are very close to those of a cranefly. Moreover, r_{A} and Φ are set to be 11 and 120deg, respectively, which are in the range of the values for actual insects [2, 48, 67] for geometric and dynamic similarity, as described in Sections 2.1 and 2.3, and are very close to those of a cranefly. The mass of the model wing m_{w} is divided by the wing area [25, 28] following the mass distribution along the wing chord measured for an actual insect wing [39]. Also, C_χ is given such that the amplitude of χ is approximately equivalent to that observed for an actual insect [49].

The example of the dimensional parameters corresponding to the above setup are $m_{\mathrm{w}} = 2.7\times10^{-7}$kg, Φ = 120deg, f_φ = 51Hz, and $C_\theta = 2.5\times10^{8}$deg/(Nm) for $L_{\mathrm{w}} = 1.3\times10^{-3}$m and the material properties of air ($\rho^{\mathrm{f}} = 1.205$kg/m^3, the dynamic viscosity $\nu^{\mathrm{f}} = 1.502\times10^{-5}$m^2/s), which are very close to the data of the actual cranefly [2, 38, 48, 67].

2.7 Analysis setup

The leading edge, the plate springs, and the wing plane are modeled using mixed interpolation of tensorial components shell elements [75] (Figure 5, number of nodes: 149, number of elements: 124), while the fluid domain is modeled using stabilized linear equal–order–interpolation velocity–pressure elements [76] (Figure 6, number of nodes: 46,920, number of elements: 254,592). Δt is set at $1/f_\varphi/5{,}000$.

The present setup for the domain size, the boundary condition, and the mesh size is almost equivalent to that in Refs. [25] and [28]. Furthermore, the present nondimensional parameters, which measure the magnitude of the interaction quantitatively, are very close to those in Refs. [25] and [28]. The present simulation software system was carefully validated

in Refs. [25] and [28]. Furthermore, it was validated using the several problems including the typical benchmark problems in the area of the finite element method [46, 47] and the other type of experiment [77]. Therefore, the present simulation software system can analyze the problem in the present study accurately.

In the computational environment of a multi-core processor (8-core Xeon 3.3GHz × 4CPUs, 64GB shared memory), the performance of the parallel computation in Section 2.5 is examined as follows: The number of fluid subdomains N_d is set as 10, 16, 20, and 36. The present parallel efficiency and speed-up are 98% and 9 times for $N_d = 10$, 93% and 14 times for $N_d = 16$, 88% and 16 times for $N_d = 20$, and 76% and 22 times for $N_d = 32$, respectively.

The reduction of the parallel efficiency for the larger N_d is because of the following reason. The present parallel computation in Section 2.5 parallelizes the computation for the pressure Poisson equation (7), which has the degrees of freedoms of the fluid domain. On the contrary, it does not parallelize the computation for the equilibrium equations (6) and (8), which have the degrees of freedoms of the structure and the fluid-structure interface. Therefore, the structural computation time relatively increases compared with the fluid computation time as N_d increases.

3. RESULTS AND DISCUSSION

3.1 Change of wingtip path mode

Let us consider symmetric flapping as the case in which $t_a^u = t_a^d = T_\varphi/8$, as shown in Figures 3(a), 3(b), and 3(c). The natural frequency f_χ^n of the elevation of the wing is changed by changing C_χ. Figure 7 shows the wing motion during one cycle for the case of $f_\chi^n = 2.8 f_\varphi$. As shown in this figure, the present pitch vibration caused by the fluid-structure interaction exhibits a characteristic pitch motion similar to insect flapping flight; i.e., the wing exhibits a high angle of attack in the middle of each half-stroke and rotates quickly upon stroke reversal.

Figure 8 shows the time histories of χ for various values of f_χ^n. χ as a function of time seems to be not entirely periodic irrespective of the periodic flapping. This might come from incommensurate natural frequencies and the lack of structural damping. However, the specific modes appear in the wingtip path as follows. Figure 9 shows the relationships between φ and χ, i.e., the wingtip paths obtained from Figure 8. Note that the value of f_χ^n is denoted by f_φ multiplied by a real number in the upper right-hand side of each figure. As shown in these figures, the mode of the two-loop with one-crossing or the figure-eight mode appears in the wingtip path for smaller f_χ^n. As f_χ^n increases, small loops appear at the both ends of the figure-eight. Finally, the four-loop with three-crossing is fully developed in these figures. The mechanism of this discontinuous mode shift for the continuous change of f_χ^n can be explained from the viewpoint of the vibration theory as follows.

The pitch angle keeps a large angle during the middle of each half stroke, where the flapping speed is constant. Therefore, the elevation component of the dynamic pressure force acting on the wing appears as shown in Figure 10. It follows that the elevation motion of the

wing can be considered as the forced vibration caused by the periodic exciting force, of which time variation follows the square of the flapping velocity.

In the symmetric flapping condition, the frequency of the periodic exciting force is $2f_\varphi$. Therefore, the vibration mode with the frequency $2f_\varphi \times n_r$ (n_r is a positive integer) closest to f_χ^n is most amplified and appears significantly in the elevation motion of the wing. Let us consider a simple sinusoidal elevation motion with frequency $2f_\varphi \times n_r$, as shown in Figures 11 (a) and (c). This motion exhibits the $2n_r$-loop mode, as shown in Figures 11 (d) and (f). Therefore, the 2-loop mode appears in the case of f_χ^n/f_φ = 2.4, 2.6, and 2.8, as shown in Figures 9 (a), (b), and (c), while the 4-loop mode appears in the case of f_χ^n/f_φ = 3.4, 3.6, 3.8, 4.0, and 4.2, as shown in Figures 9 (f), (g), (h), (i), and (j).

It is suggested that the three-loop mode can appear in the wingtip path under the asymmetric flapping condition. The aerodynamic force caused by the flapping motion has the frequency f_φ in this case, and the n_r-loop mode can appear as shown in Figures 11 (b) and (e). Let us consider asymmetric flapping as the case in which $t_a^u = T_\varphi/9$ and $t_a^d = T_\varphi/5$, as shown in Figures 3(d), 3(e), and 3(f). In the case of n_r = 2 (f_χ^n/f_φ = 2.4), the two-loop mode appears in the wingtip path, as shown in Figure 12(a). In contrast, unlike in the symmetric flapping condition, in the cases of n_r = 3 (f_χ^n/f_φ = 2.6, 2.8, 3.0, 3.2, and 3.4), the three-loop mode appears in the wingtip path, as shown in Figures 12(b) through 12(f), respectively. Furthermore, similar to the previous section, in the case of n_r = 4 (f_χ^n/f_φ = 3.6, 3.8, 4.0, and 4.2), the four-loop mode appears in the wingtip path, as shown in Figures 12(g) through 12(j), respectively. These results indicate that, in general, the n_r-loop mode can appear in the wingtip path for the case in which f_χ^n/f_φ is approximated by n_r.

The insects can control the characteristic mode of the wingtip path [5]. One explanation is that the elevation motion of the wing is directly given by the insect's own muscles at the base of the wing such that it appears [2]. The other possible explanation based on these results is that the elevation motion of the wing is given by the FSI passively, and the insect changes the flexibility at the base such that the characteristic mode appears in the wingtip path.

3.2 Lift change due to mode shift

The setup of the symmetric flapping described in the previous section is used in this section. Figure 13 shows the relationship between the frequency ratio f_χ^n/f_φ and the ratio of the mean speed of the wingtip and the mean flapping speed. Figure 14 shows the relationship between f_χ^n/f_φ and the mean nondimensional lift F_L. As shown in Figure 13, the mean speed of the wingtip increases as f_χ^n becomes larger than $3.2f_\varphi$. As shown in Figure 14, irrespective of this increase, the mean lift decreases significantly. This phenomenon can be explained as follows.

Let us consider $f_\chi^n = 2.8f_\varphi$ and $4.0f_\varphi$ as typical cases of the two-loop and four-loop modes, respectively. Figure 15 shows the time histories of the stroke angular displacement φ, the elevation angle χ, the pitch angular displacement θ, and the nondimensional lift F_L. Figures 16 through 18 show the flow fields around the wing on a cylindrical plane for the period from 9.15 cycles to 9.58 cycles.

As shown in Figure 16, the LEV can be clearly observed in the cases of $f_\chi^n = 2.8f_\varphi$ and $4.0f_\varphi$ until approximately 9.2 cycles. As shown in Figure 16(a), in the case of $f_\chi^n = 2.8f_\varphi$, the LEV maintains sufficient momentum until 9.25 cycles, which is time instant of the stroke reversal. In contrast, as shown in Figure 16(b), in the case of $f_\chi^n = 4.0f_\varphi$, the momentum of the LEV decreases quickly after approximately 9.2 cycles.

The reason why the momentum of the LEV is sufficiently maintained in the case of $f_\chi^n = 2.8f_\varphi$, irrespective of the flapping speed reduction of the wing due to stroke reversal, as shown in Figure 15(a), is that the velocity of the elevation motion of the wing remains positive until 9.25 cycles, as shown in Figure 15(b). In contrast, in the case of $f_\chi^n = 4.0f_\varphi$, because of the change from positive to negative of the velocity of the elevation motion of the wing during the period from 9.2 cycles to 9.25 cycles, as shown in Figure 15(b), the LEV does not sufficiently maintain its momentum until 9.25 cycles following the reduction in the flapping speed of the wing due to stroke reversal. Therefore, as shown in Figure 17(a), in the case of $f_\chi^n = 2.8f_\varphi$, the LEV from the previous half-stroke can obviously remain in the wake of the wing after stroke reversal, whereas in the case of $f_\chi^n = 4.0f_\varphi$, such a vortex does not appear, as evidenced by Figure 17(b).

A new LEV develops at the beginning of the next half-stroke. As shown in Figure 18, during this period, the new LEV in the case of $f_\chi^n = 2.8f_\varphi$ develops quickly, as compared to that in the case of $f_\chi^n = 4.0f_\varphi$. This is because the new LEV will be enhanced by the old LEV from the previous half-stroke, as shown in Figure 18(a). As shown in this figure, the old LEV with counterclockwise rotation induces the flow above the leading edge to form the new LEV with clockwise rotation. In contrast, in the case of $f_\chi^n = 4.0f_\varphi$, such an effect cannot be observed in Figure 18(b) because of the lack of the old LEV. Therefore, the lift in the case of $f_\chi^n = 2.8f_\varphi$ is larger than that in the case of $f_\chi^n = 4.0f_\varphi$ at the first half of each half-stroke.

The LEVs in both cases are sufficiently developed and are stable in the middle of each half-stroke. During this period, pitch angle is one of the dominant parameters of lift [78]. Therefore, the increase and decrease in lift in the case of $f_\chi^n = 4.0f_\varphi$ clearly follow the increase and decrease of the pitch angle, respectively, as shown in Figures 15(c) and 15(d). Furthermore, the increase and decrease of the pitch angle will be caused by the elevation motion of the wing, because the increase of χ and the decrease of θ from approximately 9.35 cycles are clearly interrelated and the decrease of χ and the increase of θ from approximately 9.45 cycles are clearly interrelated.

In summary, the upward elevation motion of the wing in the two-loop mode acts on the LEV so as to keep its momentum upon stroke reversal, and this LEV can remain in the wake of the wing after stroke reversal and enhance the next LEV. Because of this effect, the lift increases significantly as the mode of the wingtip path shifts to the two-loop mode in Figure 14.

4. CONCLUDING REMARKS

It was first reported that the characteristic wingtip path, such as a figure-eight, can be

created by the FSI in the present study. A flapping model wing with two lumped flexibilities describing the elevation motion and pitching motion of the wing interacting with the surrounding air was analyzed by direct numerical simulation using the three-dimensional FEM for the FSI. This simulation was guided by the dynamic similarity law for the FSI in order to accurately incorporate the data for an actual insect. A parallel computation algorithm was used to perform the systematic parametric study.

In the elevation motion of the simulated wing, the path of the wingtip exhibited characteristic modes such as the figure-eight mode. This motion can be considered as the forced vibration caused by the periodic exciting force, of which time variation follows the square of the flapping velocity. Therefore, this motion was modulated using the parameters of the flapping motion and the elevation flexibility.

In the case of the frequency ratio f_χ/f_φ approximately equal to n_r, the elevation motion of the wing presents a wingtip path with an n_r-loop mode, since the vibration mode with the frequency $n_\mathrm{r}\times f_\varphi$ is most amplified. For example, in the case of f_χ/f_φ approximately equal to 2, the two-loop mode, i.e., the figure-eight mode, appeared in the wingtip path.

In the case of the figure-eight mode, the upward elevation motion of the wing acted on the LEV so as to maintain its momentum during stroke reversal. Therefore, the old LEV from the previous half-stroke remained in the wake of the wing after stroke reversal and enhanced the development of the new LEV in the beginning of the next half-stroke. Because of this effect, the lift increased significantly as the wingtip path mode shifted to the figure-eight mode.

The controllability of the lift force in insects found in the present study is summarized as follows: The interaction of the flapping wing of the insect and the surrounding fluid causes the wingtip path. The insect can shift its characteristic modes using the flexibility at the base of the wing in order to control the lift force. Compared to previous approaches that prescribe entire wing motions in MAVs, this finding will reduce the electromechanical complexity of the flapping device.

ACKNOWLEDGEMENT

The present study was supported by JSPS KAKENHI Grant Number 17H02830.

APPENDIX

If the plate spring has the chord-wise length enough shorter than the span-wise length, the bending will be almost uniform along the span-wise direction. In this case, the plate spring works such that it is consistent with the lumped torsional flexibility, since the pitch angle of the stiff wing plate is almost uniform along the span-wise direction. In the present results, the time histories of the pitch angles at the wing's tip, middle, and root positions are indistinguishable from each other as shown in Figure A1. It follows that the chord-wise length of the plate spring in Figure 5 is adequately selected.

If the position of the rotational axis is sufficiently close to the leading edge, or the span-wise length of the plate spring is sufficiently short, this selection will not affect the lift and the drag significantly [22]. Approximately 40% increase of the chord-wise length of the plate spring in Figure 5 slightly perturbs the time histories of the pitch and elevation angles, but it has little effect on the mode of the wingtip path as shown in Figure A2. In this validation, the Young's modulus E of the plate spring is changed such that the torsional spring constant G, which is the inverse of C_θ, keeps the value constant using the following equation [25] as $G = E\,I\,/\,l_c$, where the second moment of the section $I = l_w\,t^3/12$, l_w and t are the span-wise length and the thickness of the plate spring, respectively, and l_c is the chord-wise length of the plate spring. It follows that the chord-wise length of the plate spring in Figure 5 is adequately selected such that it doesn't change the conclusion of this study.

FIGURES

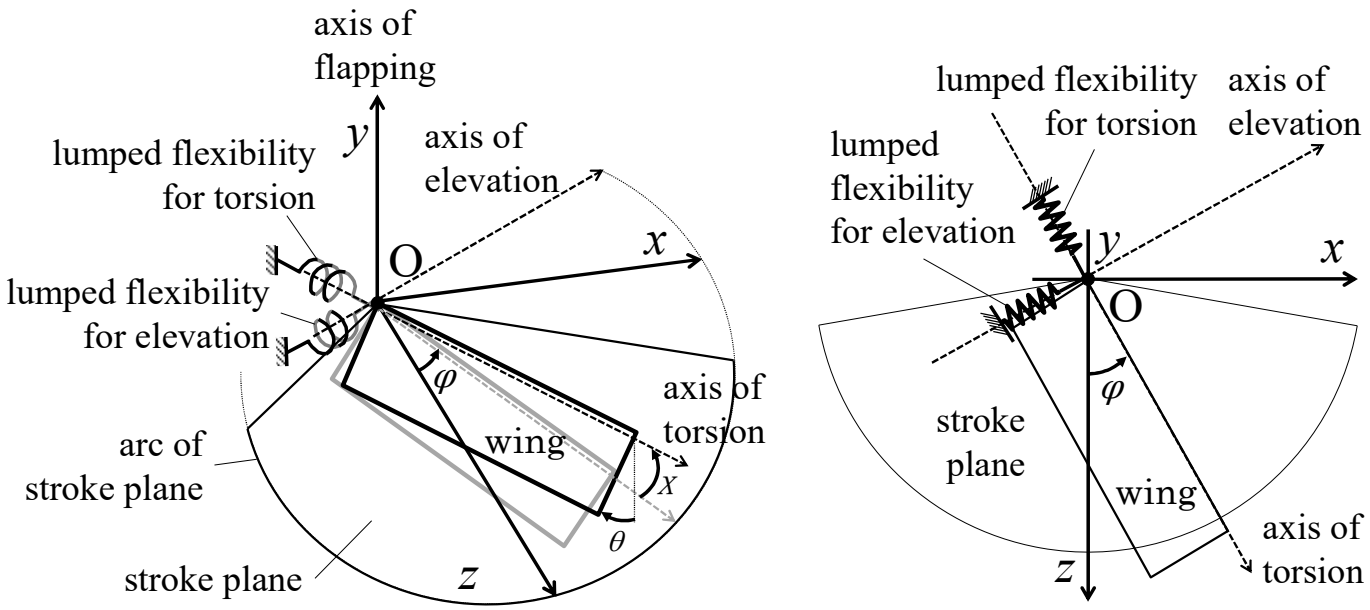

(a) bird's-eye view

(b) *xz*-plane view

Figure 1 Extended lumped flexibility model, where the conventional model with lumped torsional flexibility only is extended so as to allow the wing's elevation motion from the stroke plane. The flexibility of the wing with respect to elevation from the stroke plane is modeled using the lumped flexibility at the base of the wing, which is expressed schematically as a spring. The wing base is placed at the origin O of a Cartesian coordinate system. The horizontal *x*-axis is positive in the forward direction of the longitudinal axis of the insect body. The stroke plane is set in the horizontal *xz* plane. The flapping axis coincides with the vertical *y*-axis, and φ is the angular displacement of the flapping motion. The axis of the torsion is placed along the leading edge, and θ is the pitch angular displacement. The axis of the elevation is placed in the stroke plane and is normal to the axis of torsion, and χ is the elevation angular displacement.

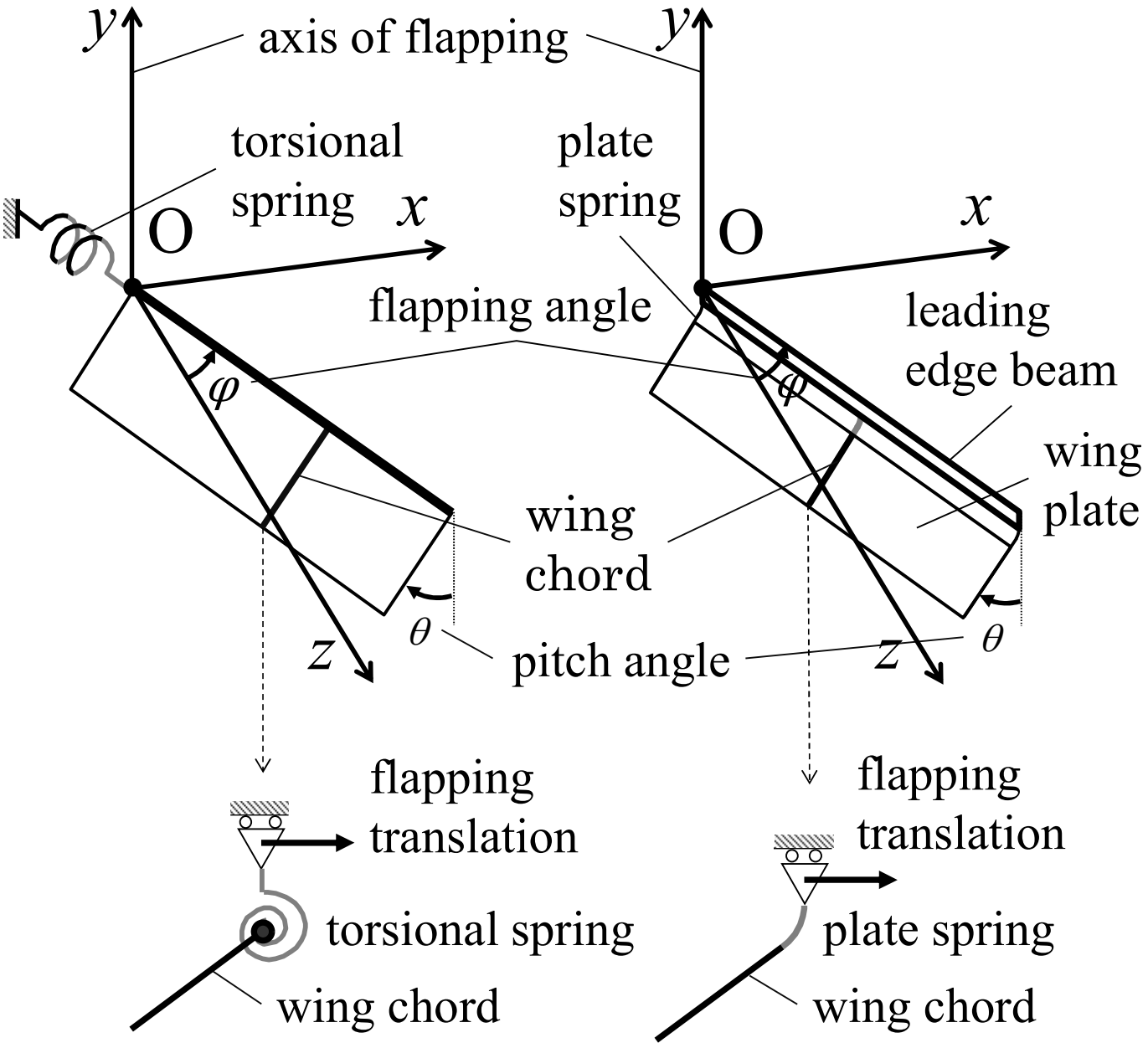

(a) Lumped torsional flexibility using torsional spring (b) Lumped torsional flexibility using plate spring

Figure 2 Implementation of the lumped torsional flexibility. In the left figure (a), the torsional spring is used to illustrate the concept of the lumped torsional flexibility. In the right figure (b), it is replaced with the plate spring as its implementation. The stiff leading edge beam and wing plate are connected by the flexible plate spring. The wing plate occupies a large part of the model wing. The plate spring works as the lumped torsional flexibility, since the plate spring is narrow.

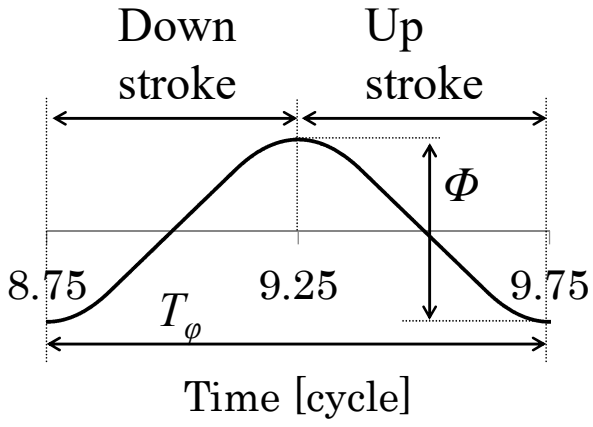

(a) Stroke angular displacement ($t_a^u = t_a^d = T_\varphi/8$)

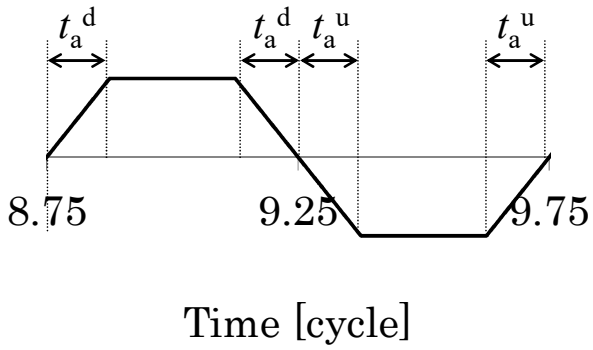

(b) Stroke angular velocity ($t_a^u = t_a^d = T_\varphi/8$)

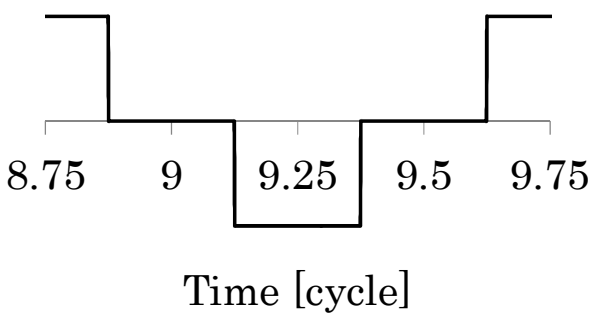

(c) Stroke angular acceleration ($t_a^u = t_a^d = T_\varphi/8$)

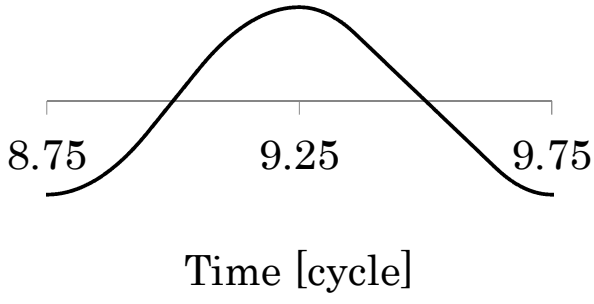

(d) Stroke angular displacement ($t_a^u = T_\varphi/9$, $t_a^d = T_\varphi/5$)

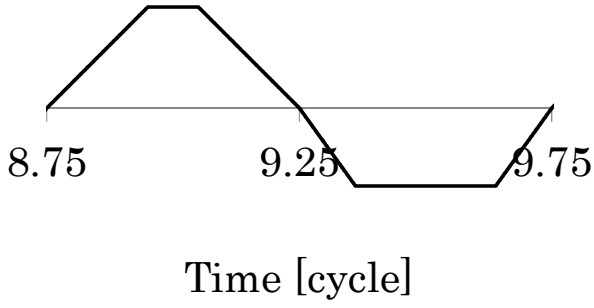

(e) Stroke angular velocity ($t_a^u = T_\varphi/9$, $t_a^d = T_\varphi/5$)

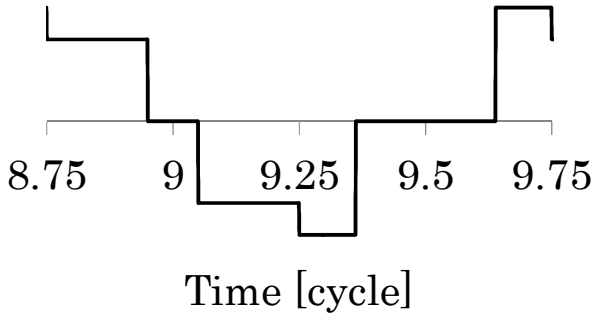

(f) Stroke angular acceleration ($t_a^u = T_\varphi/9$, $t_a^d = T_\varphi/5$)

Figure 3 Modeling of flapping motion. The time variation of φ is close to sinusoidal but has a larger acceleration or deceleration during stroke reversals and a constant velocity during the middle of each half-stroke. The time variation of $d\varphi/dt$ is expressed as a trapezoidal function, where the acceleration or deceleration time t_a is used to define the period of increasing or decreasing of the flapping velocity in each cycle, and t_a^u and t_a^d are for the upstroke and the downstroke, respectively. T_φ is the flapping period, which is the inverse of the flapping frequency f_φ. Φ is the stroke angle.

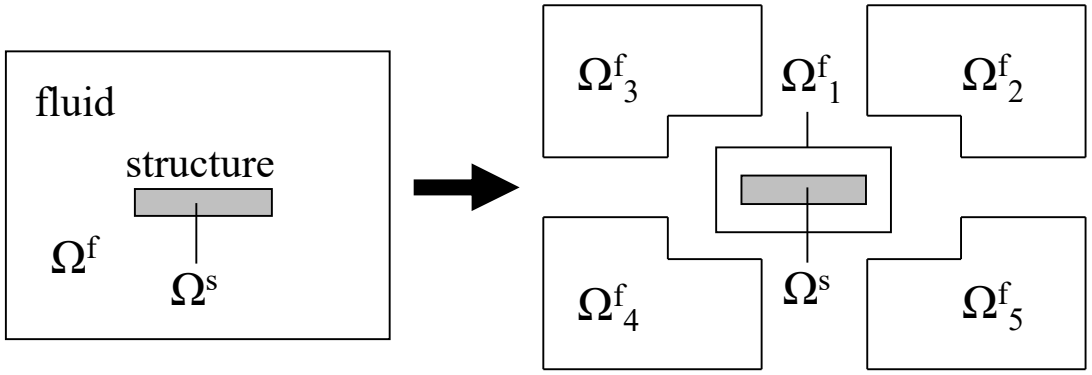

Figure 4 Schematic view of domain decomposition.

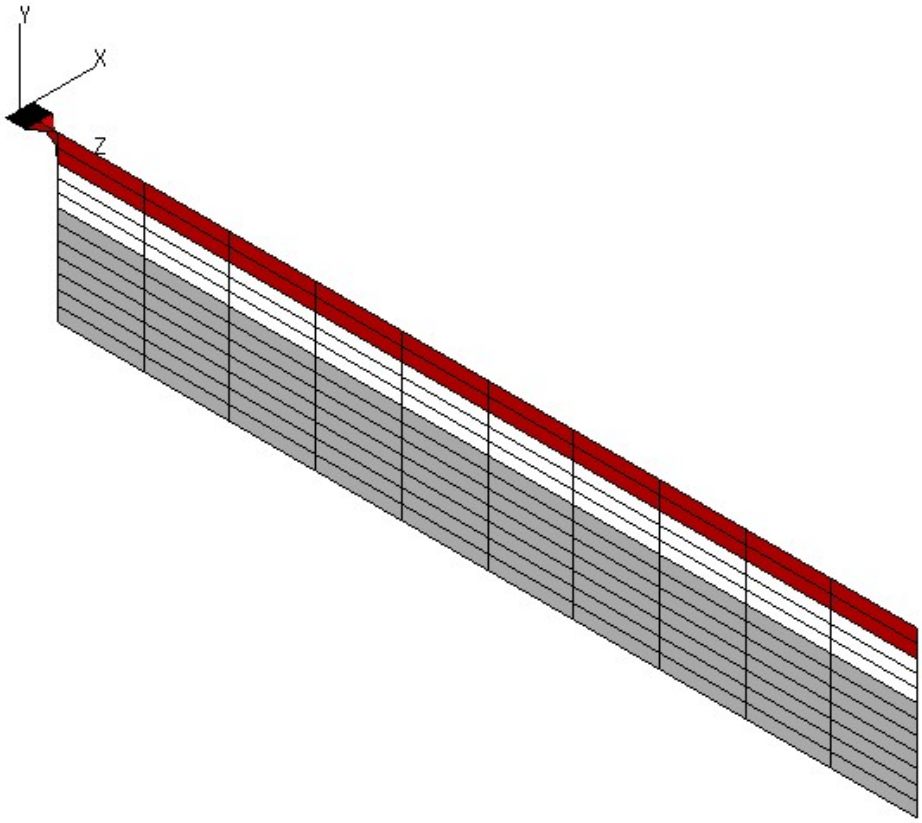

Figure 5 Finite element mesh of the model wing. The white domain is the plate spring for the concentrated torsional flexibility, the black domain is the plate spring for the concentrated elevation flexibility, the grey domain is the stiff wing plate, and the red domain is the stiff leading edge. The chord-wise lengths of the leading edge, the plate spring, and the wing plate are set as 16%, 23%, and 61%, respectively, of the total chord length.

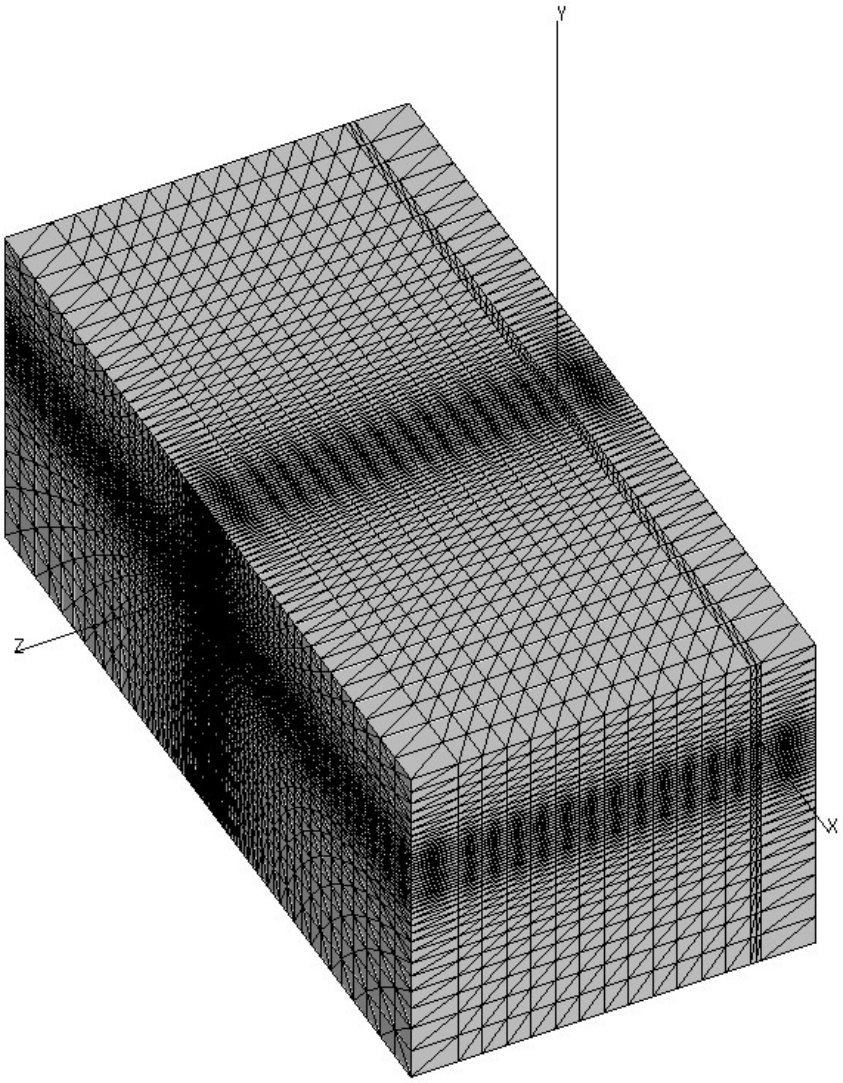

Figure 6 Finite element mesh of the surrounding fluid.

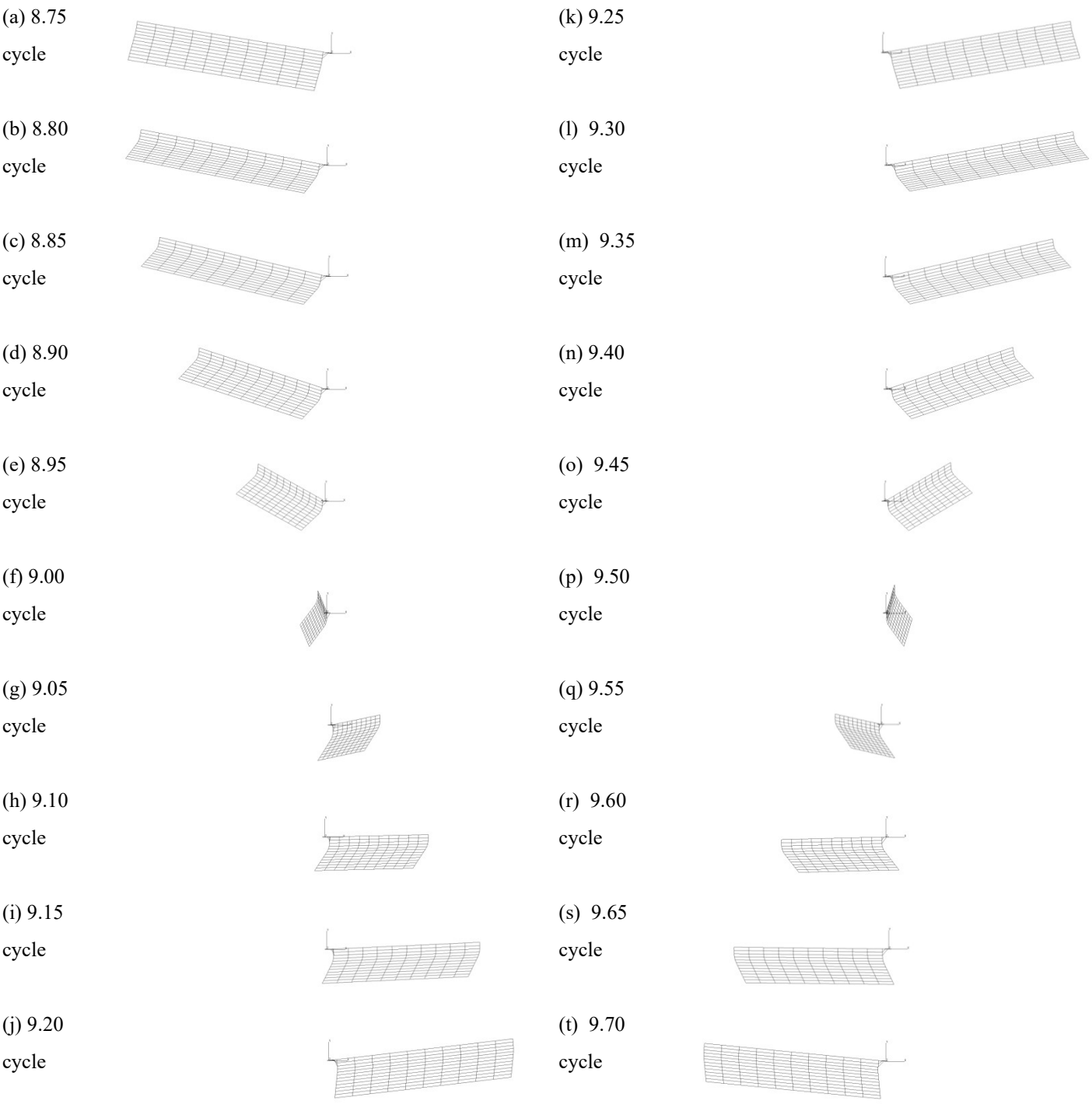

Figure 7 Wing's motion during one stroke from 8.75cycle to 9.70cycle in the case of the natural frequency of the elevation $f_{\chi}^{\mathrm{n}} = 2.8 f_{\varphi}$. The view direction is (0, 0, 1).

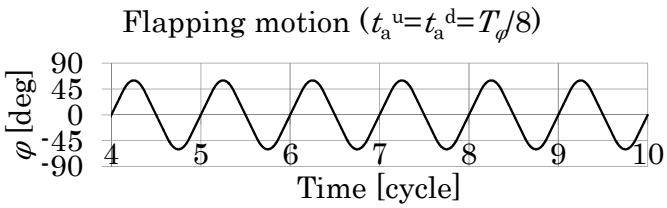

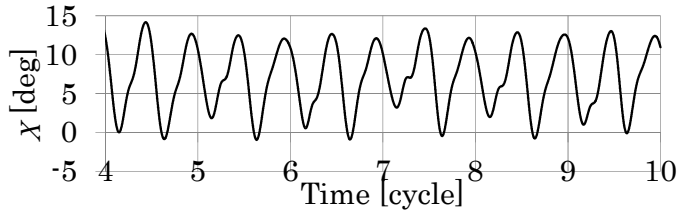

(a) $f_\chi^n = 2.4f_\varphi$

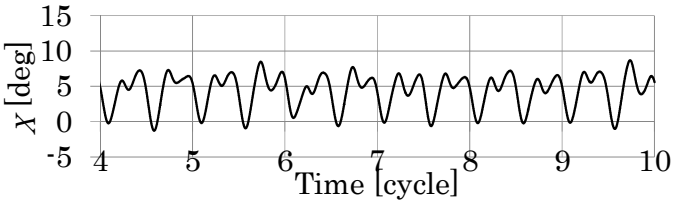

(f) $f_\chi^n = 3.4f_\varphi$

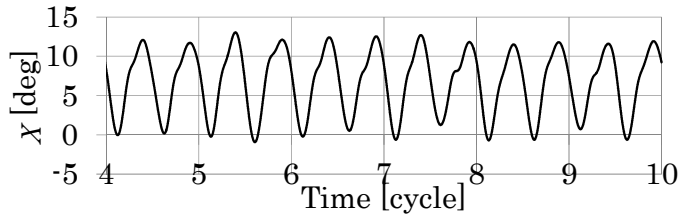

(b) $f_\chi^n = 2.6f_\varphi$

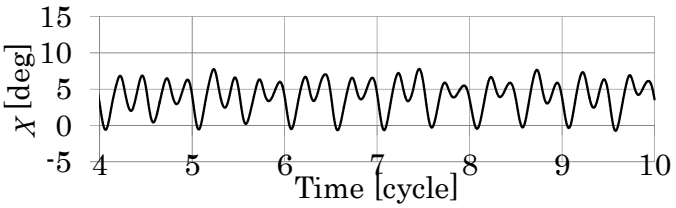

(g) $f_\chi^n = 3.6f_\varphi$

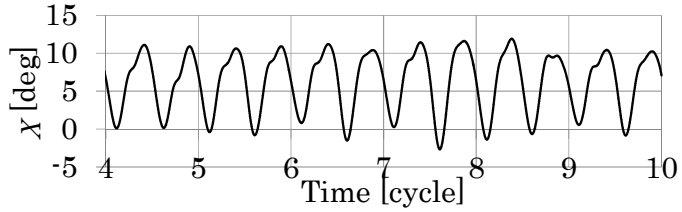

(c) $f_\chi^n = 2.8f_\varphi$

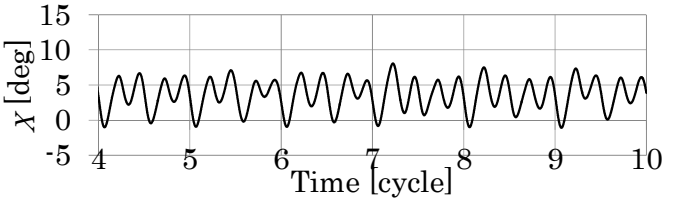

(h) $f_\chi^n = 3.8f_\varphi$

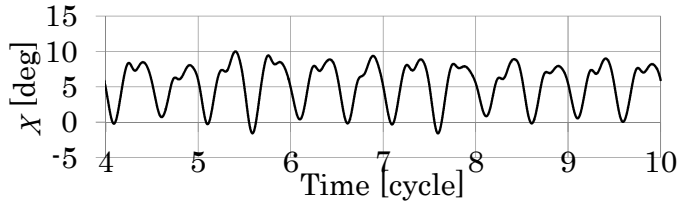

(d) $f_\chi^n = 3.0f_\varphi$

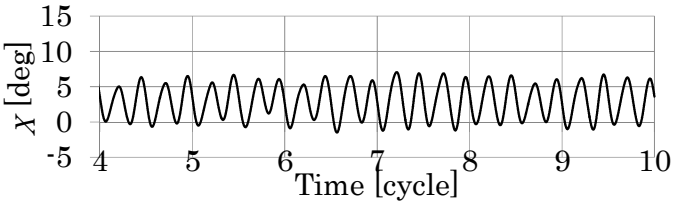

(i) $f_\chi^n = 4.0f_\varphi$

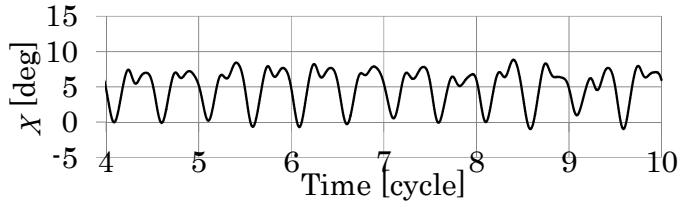

(e) $f_\chi^n = 3.2f_\varphi$

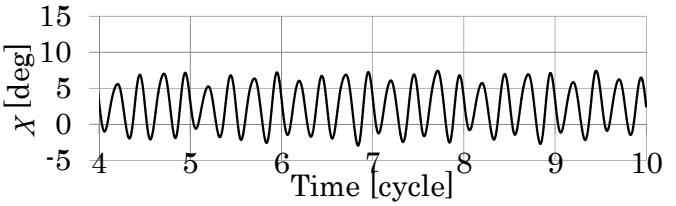

(j) $f_\chi^n = 4.2f_\varphi$

Figure 8 Time histories of the wing's elevation angle χ for the various natural frequency of the wing's elevation motion f_χ^n under the symmetric flapping condition.

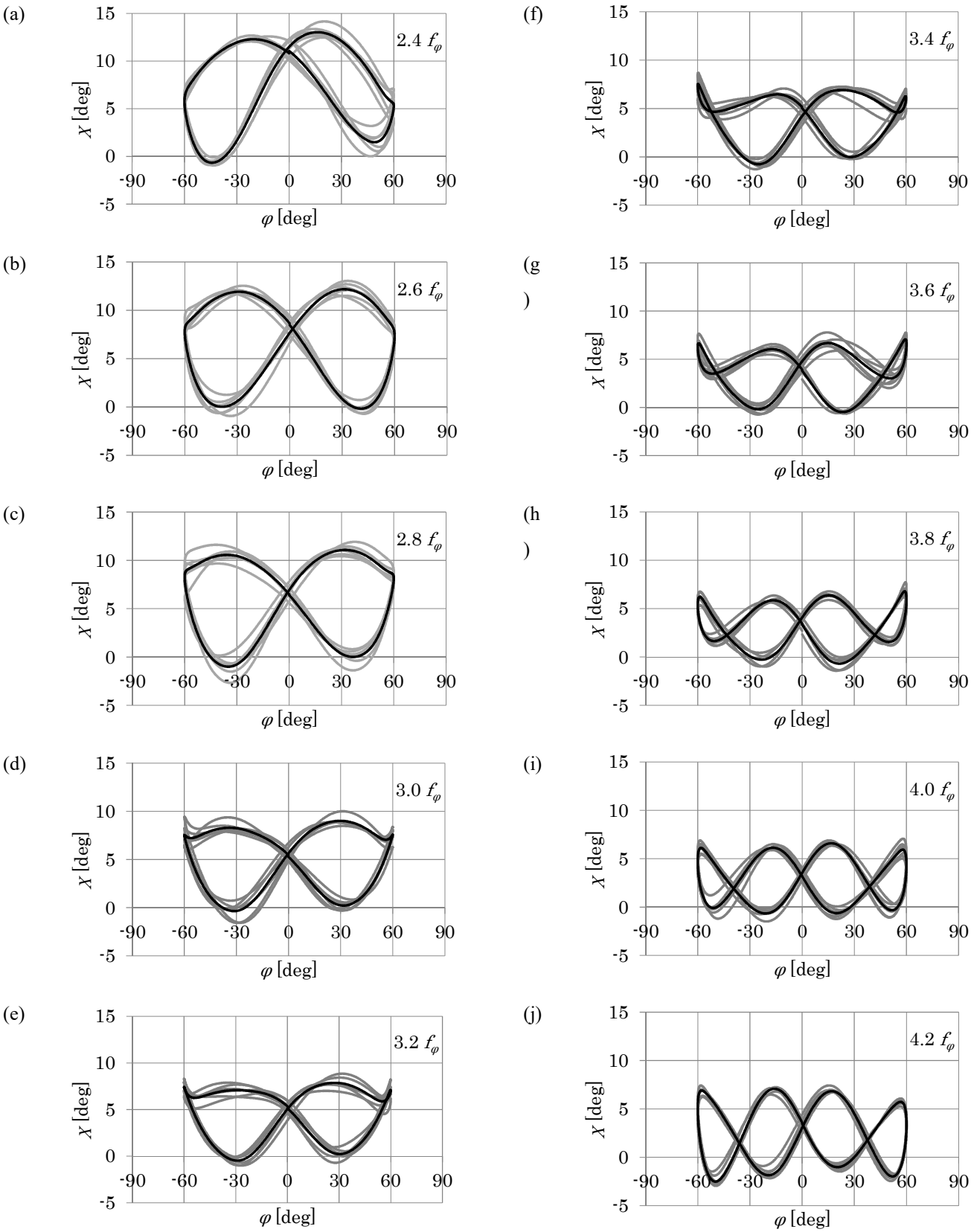

Figure 9 Trajectories of the wing tip in (φ, χ) plane, which show the mode of the tip path motion under the symmetric flapping condition. In each figure, the grey lines indicate each trajectory for n-th cycle (n = 5, …, 10), and the black line indicates the mean of them. Note that f_φ multiplied by real number in the upper right hand side of each figure denotes the value of f_χ^{n}.

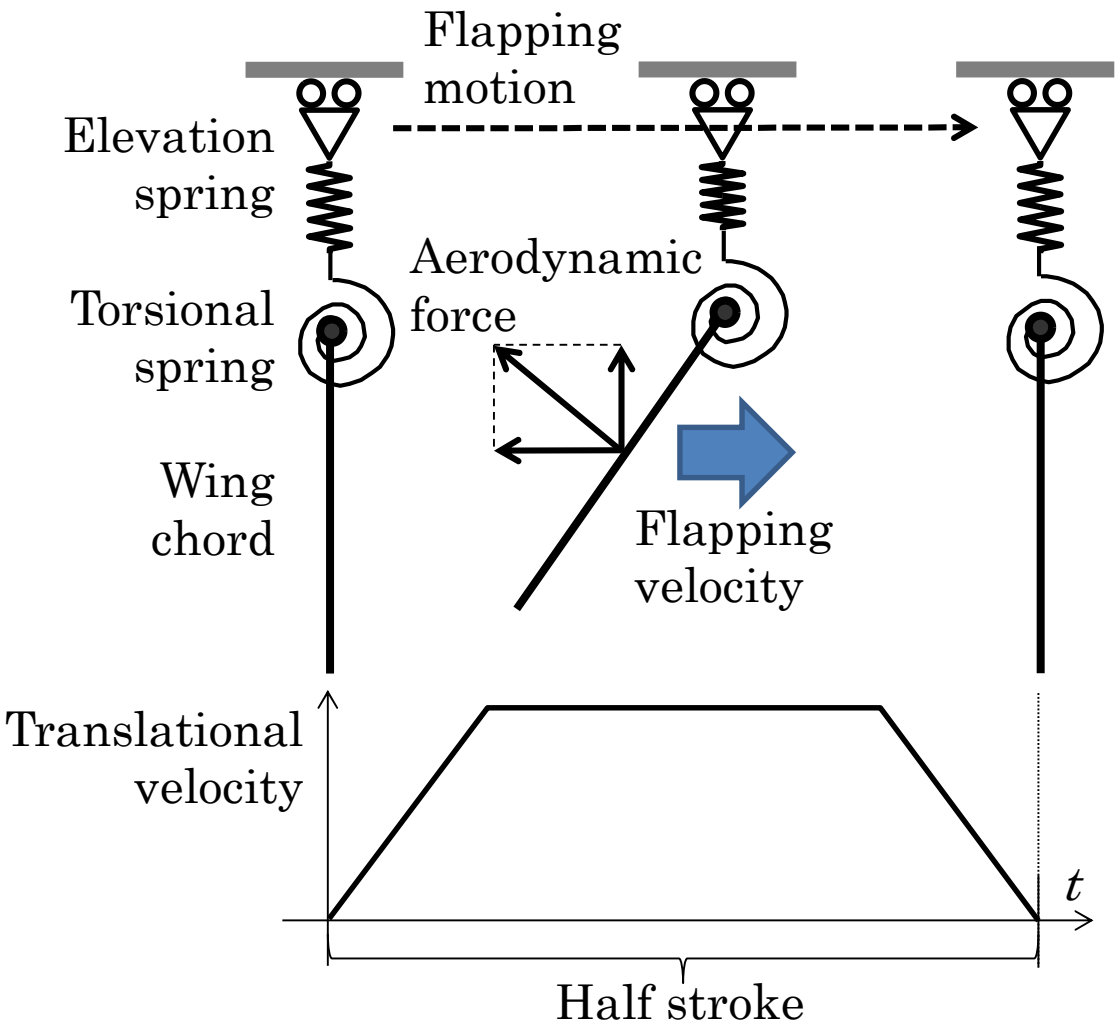

Figure 10 Schematics showing the aerodynamic force acting on the wing during the middle of each half stroke. The pitch angle keeps a large angle during the middle of each half stroke, where the flapping speed is constant. Therefore, the elevation component of the dynamic pressure force acting on the wing appears as shown in this figure.

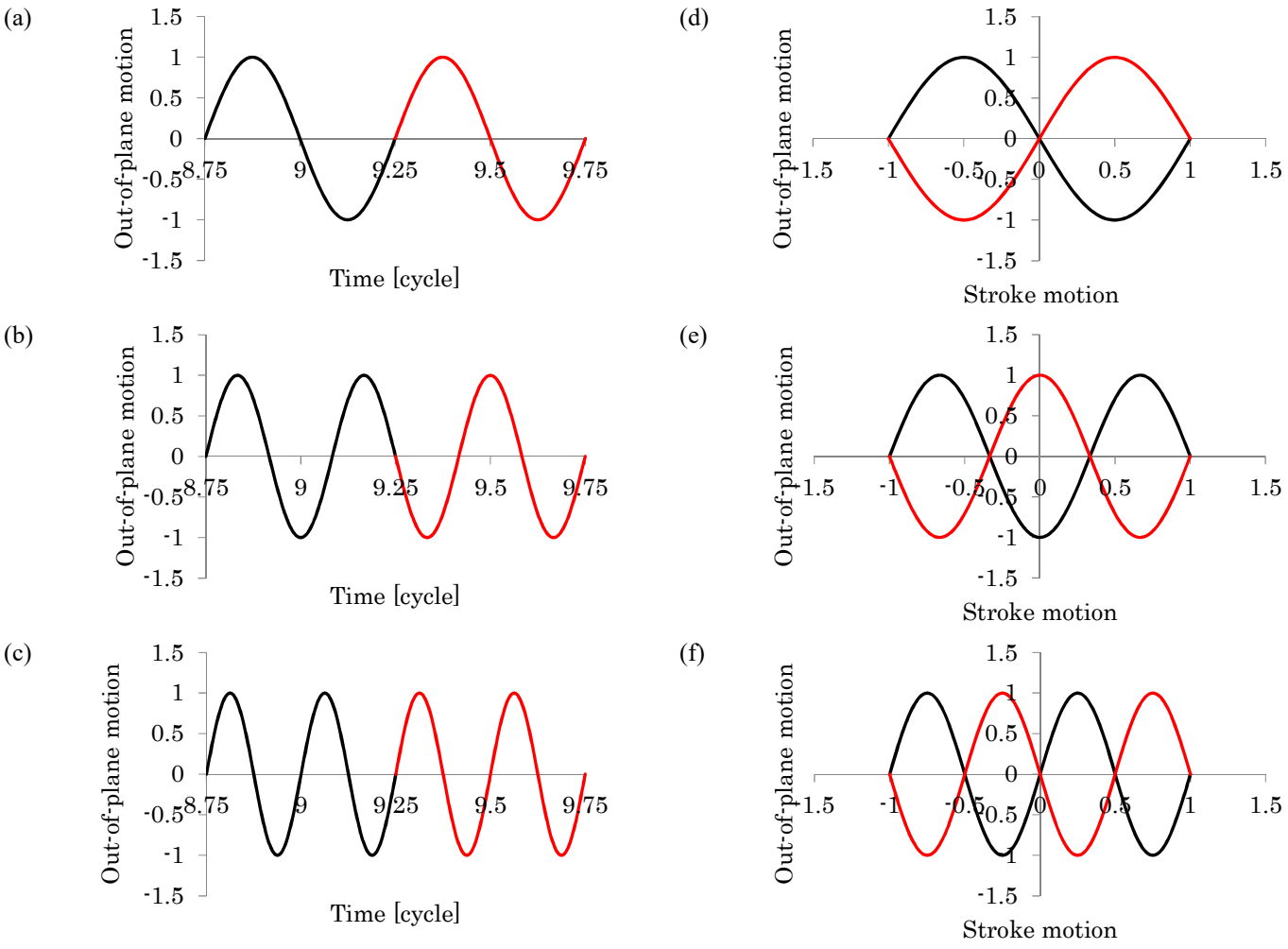

Figure 11 (a) – (c) are the time histories of the ideal wing's elevation motion, where the sinusoidal motions with the frequencies $2f_\varphi$, $3f_\varphi$, and $4f_\varphi$ are assumed, respectively, and the unit amplitude is considered. (d) – (f) are the relationships between the stroke motion and the elevation motion.

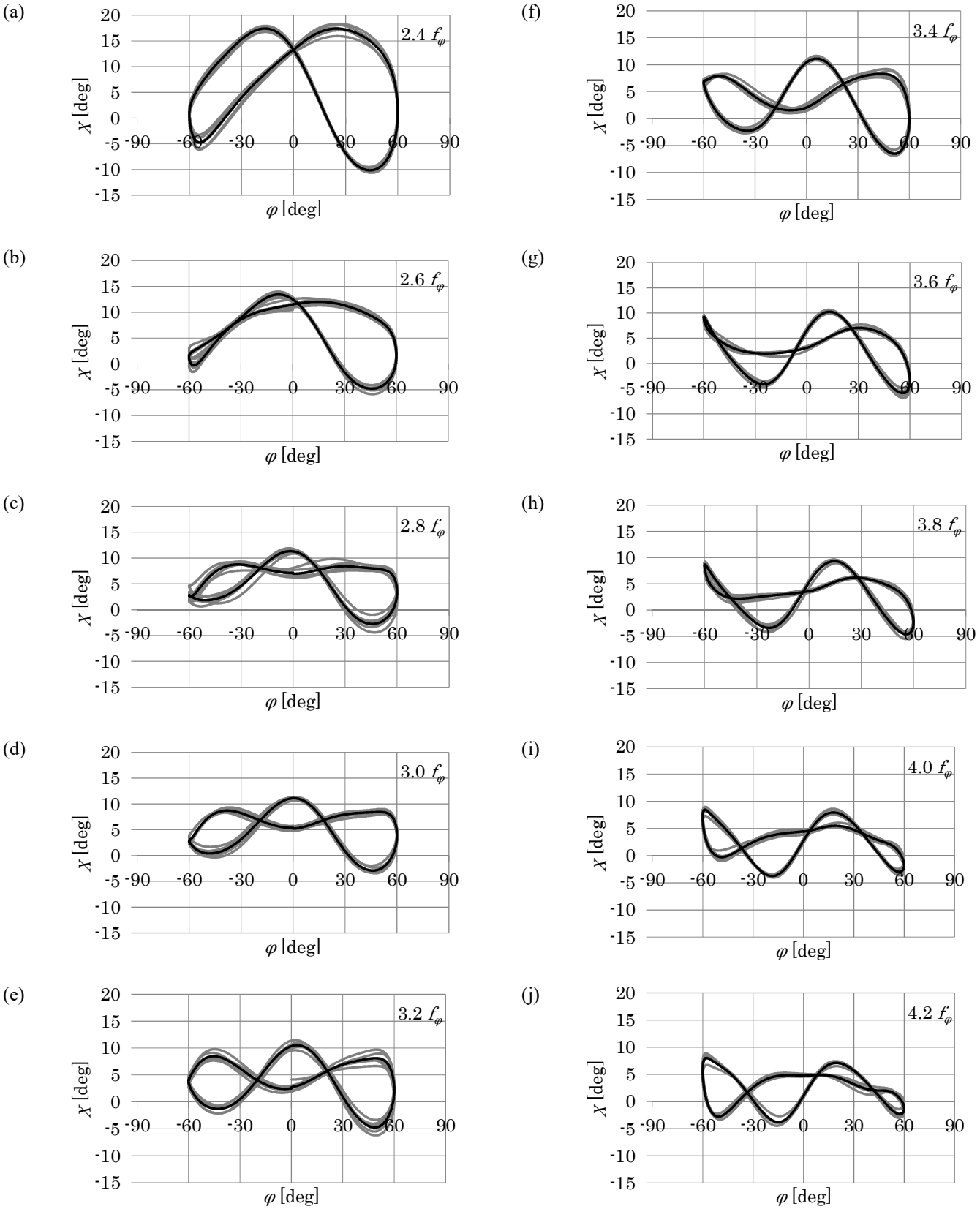

Figure 12 Trajectories of the wing tip in (φ, χ) plane, which show the mode of the tip path motion under the symmetric flapping condition. In each figure, the grey lines indicate each trajectory for n-th cycle (n = 5, …, 10), and the black line indicates the mean of them. Note that f_φ multiplied by real number in the upper right hand side of each figure denotes the value of f_χ.

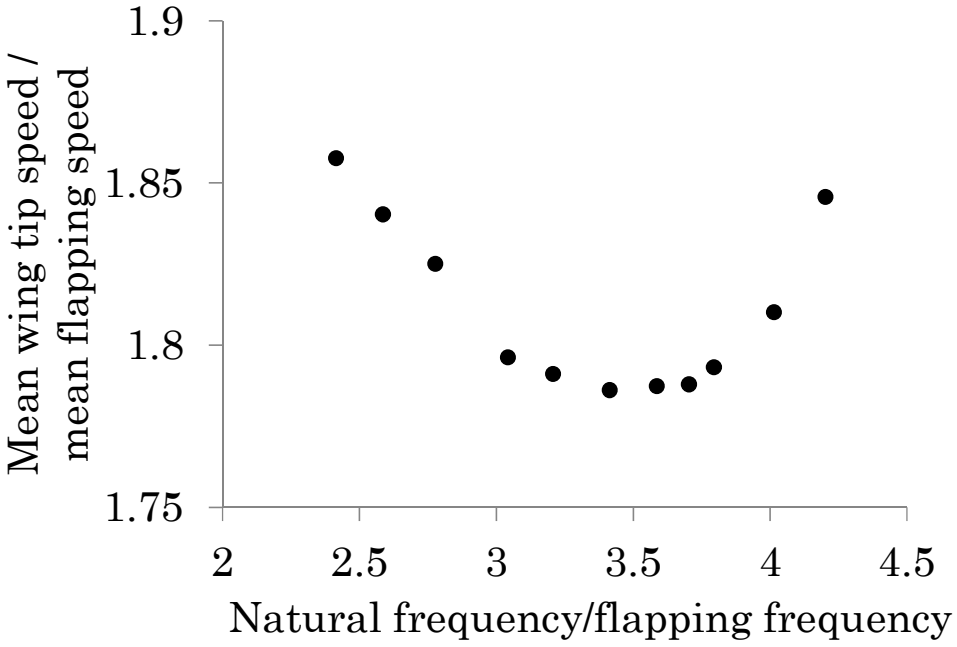

Figure 13 Relationship between $f_{\chi}^{n} / f_{\varphi}$ and the ratio of the mean wingtip speed and the mean flapping speed in the case of the symmetric flapping.

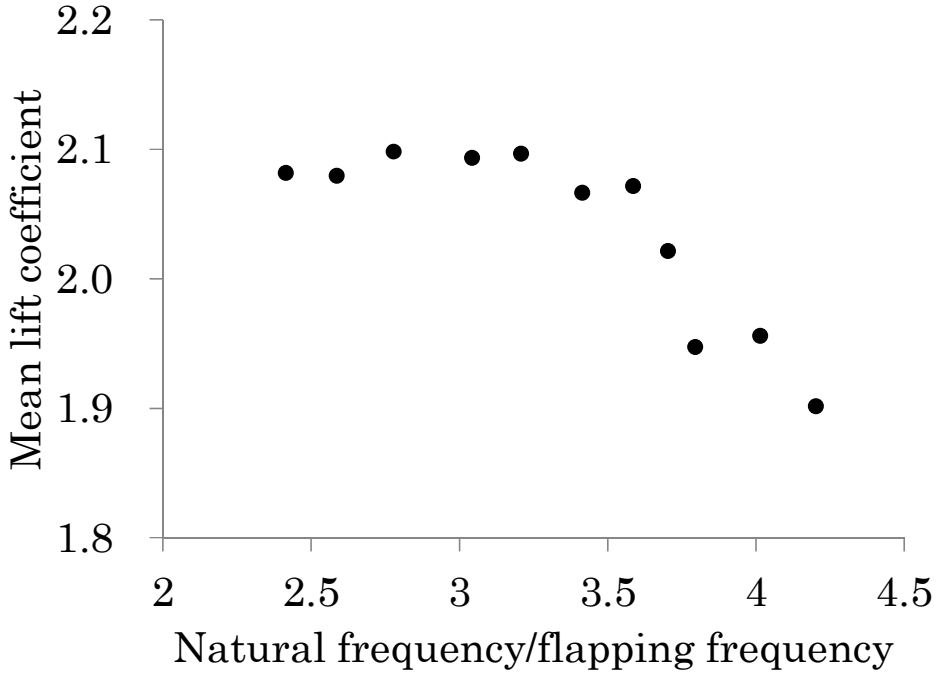

Figure 14 Relationship between $f_{\chi}^{n} / f_{\varphi}$ and the mean lift coefficient in the case of the symmetric flapping.

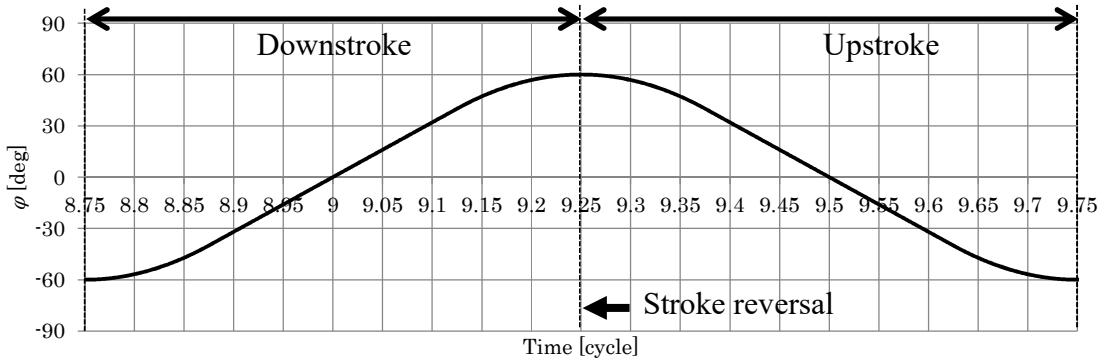

(a) The stroke angle φ

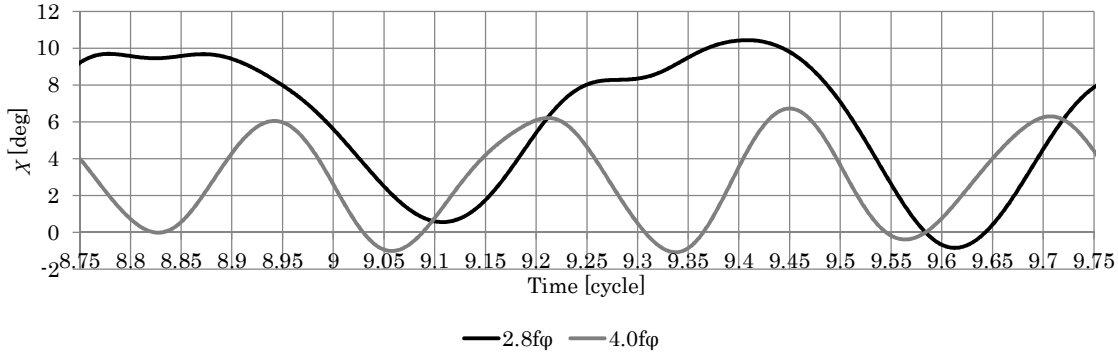

(b) The wing's elevation angle χ

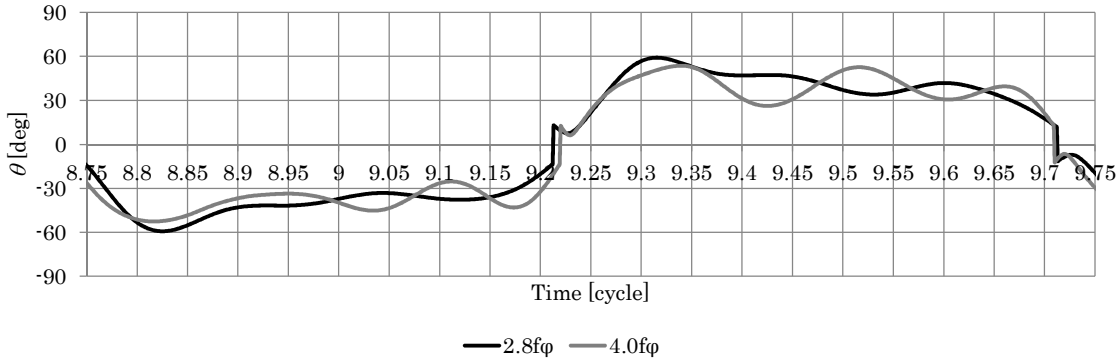

(c) The pitch angle θ

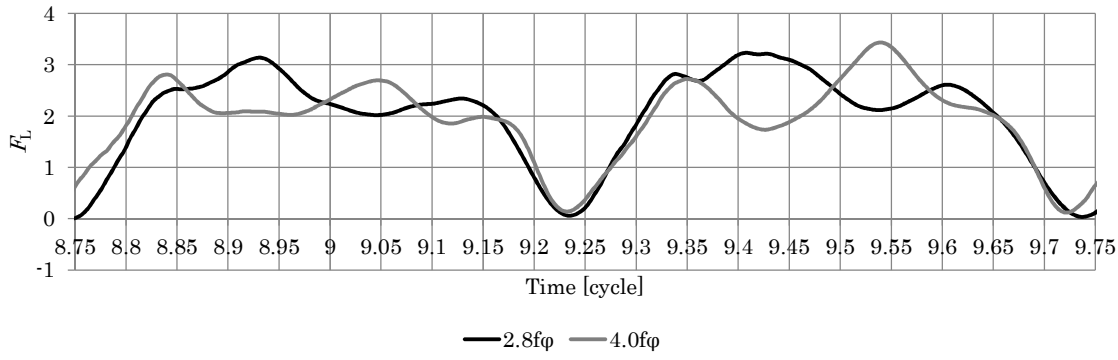

(d) The nondimensional lift F_L.

Figure 15 Time histories of the stroke angle φ, the wing's elevation angle χ, the pitch angle θ, and the nondimensional lift F_L. The black lines indicate the time histories for the $f_\chi^n = 2.8f_\varphi$, and the grey lines indicate the time histories for the $f_\chi^n = 4.0f_\varphi$.

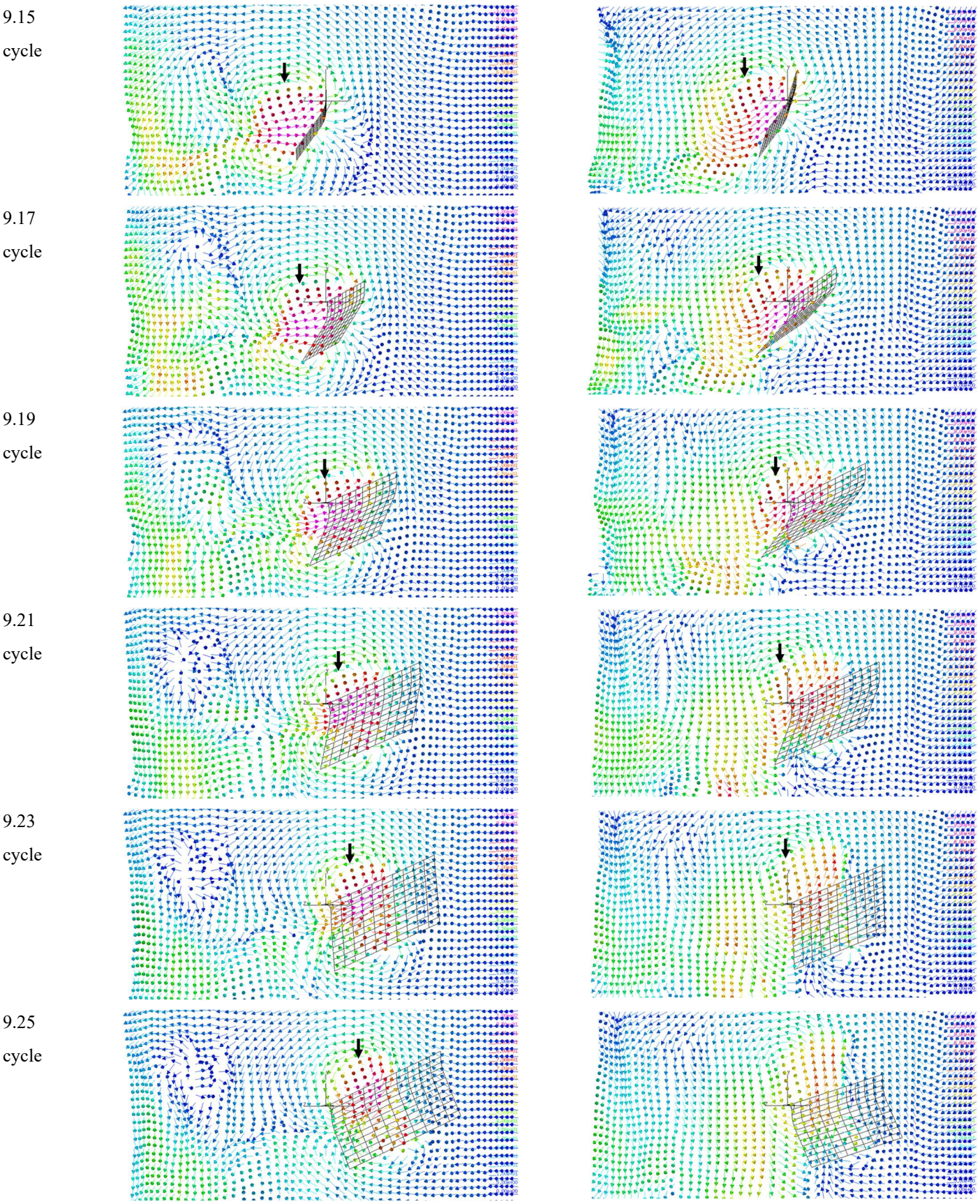

(a) $f_{\chi}^{n} = 2.8 f_{\varphi}$ (b) $f_{\chi}^{n} = 4.0 f_{\varphi}$

Figure 16 Fluid velocity field around wing from 9.15cycle to 9.25cycle on a cylindrical plane, whose radius divided by the wing longitudinal length is approximately equal to the non-dimensional radius of the second moment of the wing area $1/3^{1/2}$. Colored arrows indicate the fluid velocity and the color indicates the magnitude from from 0 (blue) to the speed three times larger than the mean flapping speed approximately (pink). The view direction is (1, 0, 1). Black bold arrow indicate the old leading edge vortex.

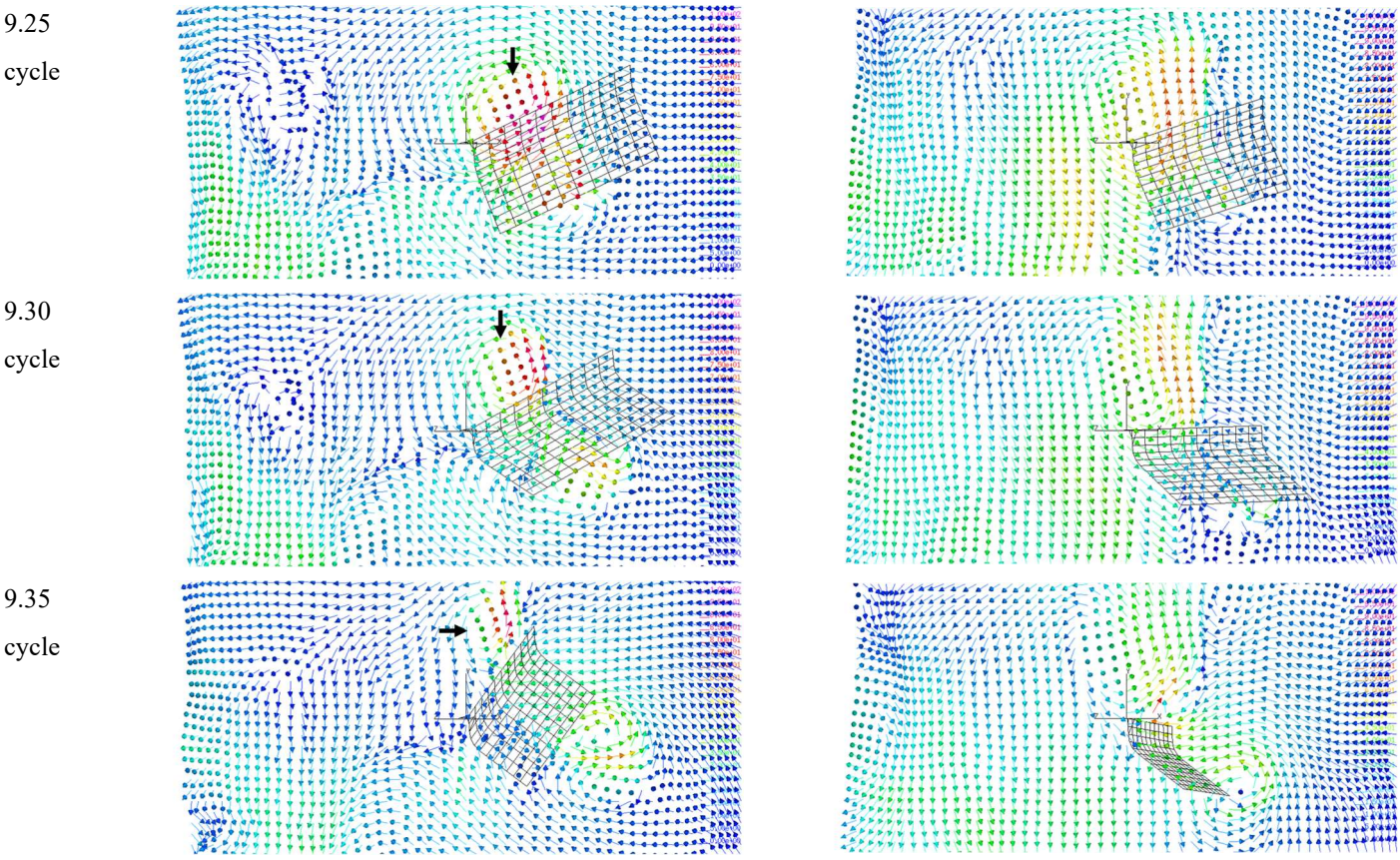

(a) $f_{\chi}^{n} = 2.8 f_{\varphi}$ (b) $f_{\chi}^{n} = 4.0 f_{\varphi}$

Figure 17 Fluid velocity field around wing from 9.25cycle to 9.35cycle on a cylindrical plane, whose radius divided by the wing longitudinal length is approximately equal to the non-dimensional radius of the second moment of the wing area $1/3^{1/2}$. Colored arrows indicate the fluid velocity and the color indicates the magnitude from from 0 (blue) to the speed three times larger than the mean flapping speed approximately (pink). The view direction is (1, 0, 1). Black bold arrows indicate the old leading edge vortex.

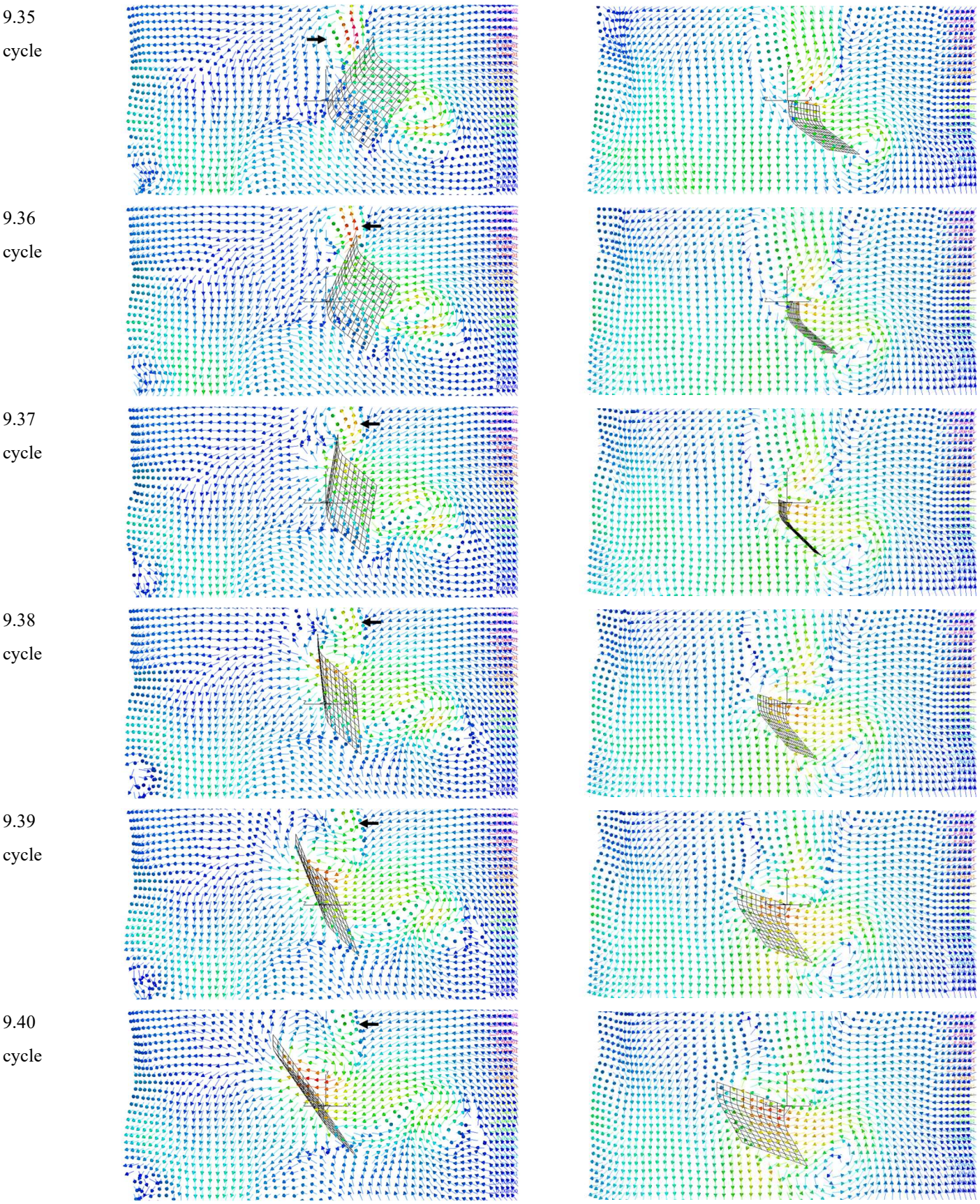

(a) $f_{\chi}^{n} = 2.8 f_{\varphi}$ (b) $f_{\chi}^{n} = 4.0 f_{\varphi}$

Figure 18 Fluid velocity field around wing from 9.35cycle to 9.40cycle on a cylindrical plane, whose radius divided by the wing longitudinal length is approximately equal to the non-dimensional radius of the second moment of the wing area $1/3^{1/2}$. Colored arrows indicate the fluid velocity and the color indicates the magnitude from 0 (blue) to the speed three times larger than the mean flapping speed approximately (pink). The view direction is (1, 0, 1). Black bold arrows indicate the old leading edge vortex.

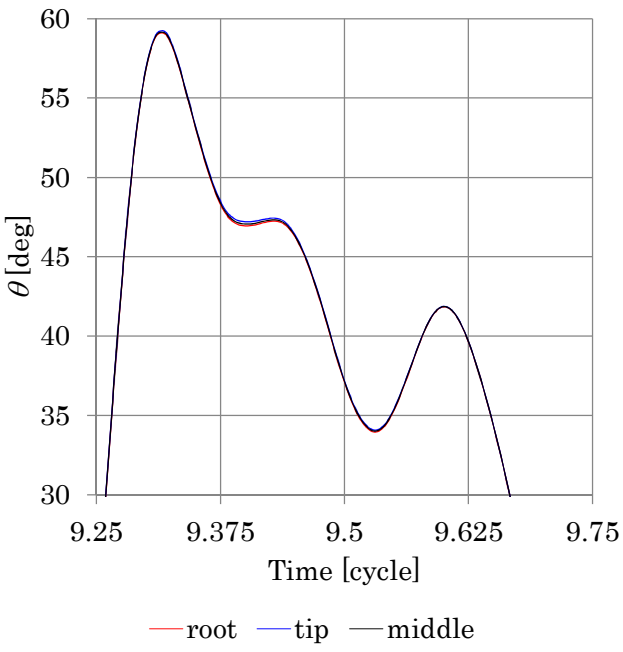

(a) $f_{\chi}^{n} = 2.8 f_{\varphi}$

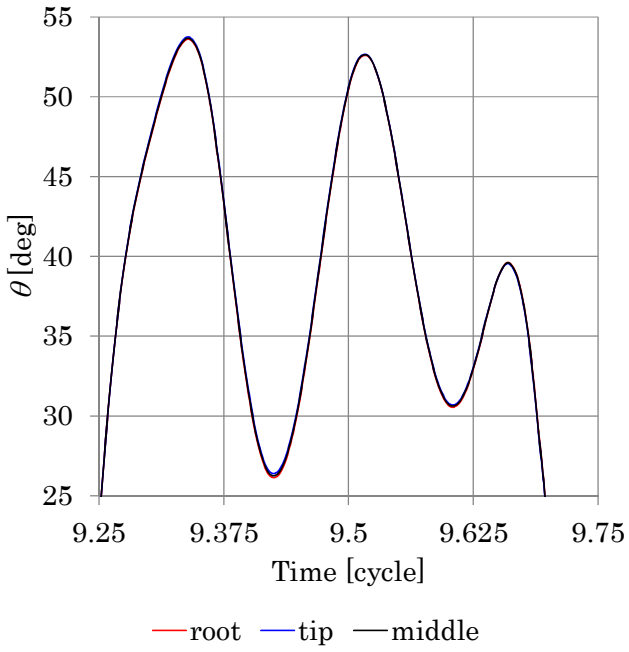

(b) $f_{\chi}^{n} = 4.0 f_{\varphi}$

Figure A1 Close-up view of the time histories of the pitch angle θ.

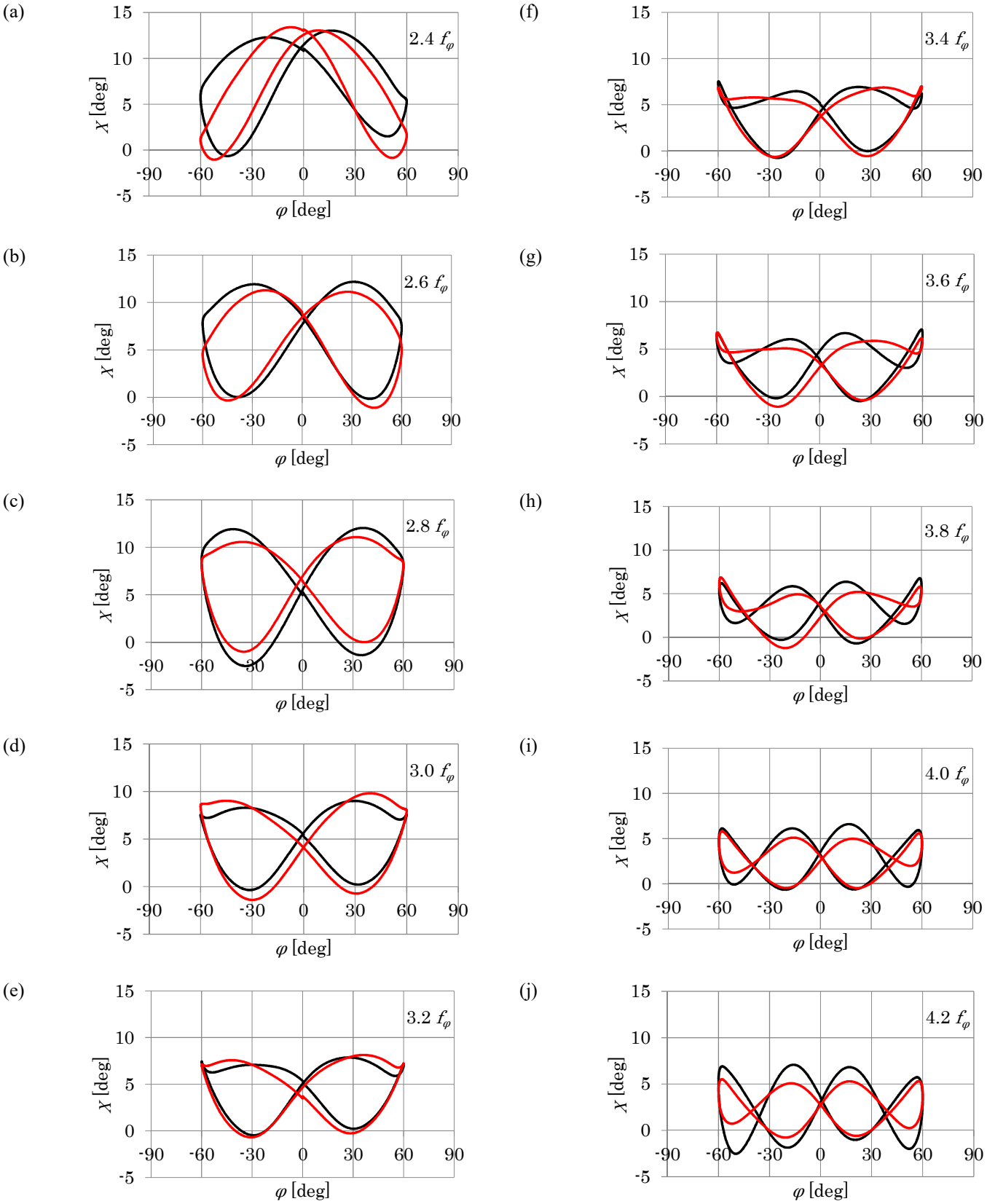

Figure A2 Influence of the chord-wise length of the plate spring on the results. In each trajectory of the wing tip in (φ, χ) plane, the black line indicates the case using the original chord-wise length of the plate spring, while the red line indicates the case using the 40% increase of the original chord-wise length of the plate spring. Each trajectory is averaged for n-th cycle (n = 5, …, 10). f_φ multiplied by real number in the upper right hand side of each figure denotes the value of f_χ^n.